J. Fluid Mech. (2014), *vol.* 743, *pp.* 399–447.
doi:10.1017/jfm.2013.681

On the microphysical behaviour of wind-forced water surfaces and consequent re-aeration

William L. Peirson[1],†, **James W. Walker**[1],‡ **and Michael L. Banner**[2]

[1]Water Research Laboratory, School of Civil and Environmental Engineering, University of New South Wales, King St, Manly Vale, NSW 2093, Australia

[2]School of Mathematics and Statistics, University of New South Wales, Sydney, NSW 2052, Australia

(Received 9 May 2011; revised 17 December 2013; accepted 23 December 2013; first published online 5 March 2014)

A detailed laboratory investigation of the mechanical and low-solubility gas coupling between wind and water has been undertaken using a suite of microphysical measurement techniques. Under a variety of wind conditions and in the presence and absence of mechanically generated short waves, approximately fetch-independent surface conditions have been achieved over short laboratory fetches of several metres. The mechanical coupling of the surface is found to be consistent with Banner (*J. Fluid Mech.* vol. 211, 1990, pp. 463–495) and Banner & Peirson (*J. Fluid Mech.* vol. 364, 1998, pp. 115–145). Bulk observations of re-aeration are consistent with previous laboratory studies. The surface kinematical behaviour is in accordance with the observations of Peirson & Banner (*J. Fluid Mech.* vol. 479, 2003, pp. 1–38). Also, their predictions of a strong enhancement of low-solubility gas flux at the onset of microscale breaking is confirmed and direct observations show a concomitant onset of very thin aqueous diffusion sublayers. It is found that the development of strong parasitic capillary waves towards the incipient breaking limit does not noticeably enhance constituent transfer. Across the broad range of conditions investigated during this study, the local instantaneous constituent transfer rate remains approximately log-normally distributed with an approximately constant standard deviation of $0.62 \pm 0.15(\log_e(\mathrm{m\ s^{-1}}))$. Although wind-forced water surfaces are shown to be punctuated by intense tangential stresses and local surface convergence, localized surface convergence does not appear to be the single critical factor determining exchange rate. Larger-scale orbital wave straining is found to be a significant constituent transfer process in contrast to Witting (*J. Fluid Mech.* vol. 50, 1971, pp. 321–334) findings for heat fluxes, but the measured effects are consistent with his model. By comparing transfer rates in the presence and absence of microscale breaking, low-solubility gas transfer was decomposed into its turbulent/capillary ripple, gravity-wave-related and microscale breaking contributions. It was found that an efficiency factor of approximately 17 % needs to be applied to Peirson & Banner's model, which is extended to field conditions. Although bulk thermal effects were observed and thermal diffusion layers are presumed thicker than their mass diffusion counterparts, significant thermal influences were not observed in the results.

Key words: Air/sea interactions, gas transfer, wind-wave interactions

†Email address for correspondence: w.peirson@unsw.edu.au

‡Present address: Sogreah Gulf – Artelia Group, PO Box 18271, Dubai, UAE.

1. Introduction

The exchanges of heat, mass and momentum across air–water interfaces involve microphysical interfacial processes that have an influence on a global scale. Exchanges at the surface of ocean waters fundamentally influence weather systems, climate change, pollutant fate and the environmental integrity of ecosystems (Donelan 1990; Wanninkhof *et al.* 2009). The exchange of low-solubility gases (particularly O_2) plays a crucial role in maintaining the integrity of aquatic environments and in the treatment of wastewaters. Present research is directed at better quantifying those processes believed to be principally responsible for air–sea gas exchange rates.

Conventionally, wind speed is the most common variable used for parameterizing constituent exchange at wind-forced interfaces in the field (e.g. Liss & Merlivat 1986; Wanninkhof 1992; Wanninkhof & McGillis 1999; Wanninkhof *et al.* 2009). When considered on the oceanic global scale, these conventional parameterizations yield global CO_2 uptakes that can vary significantly and, consequently, they are ultimately calibrated globally against historical bomb data (Wanninkhof *et al.* 2009). In the laboratory also, compilations of data as a function of wind forcing (e.g. Komori, Nagaoa & Murakami 1993, figure 8) show scatter in assembled data sets that span one order of magnitude. Donelan & Wanninkhof (2002) have observed that some of these differences may be due to uncertainty in the measurements and other factors that may affect constituent exchange.

Consequently, other empirical relationships are being developed which include the influence of key processes. Bulk parameterizations of air–water exchange of low-solubility gases have been developed based on the intensity of wind forcing, small-scale wave activity, a surface renewal statistic, surface divergence or, at higher wind forcing, changes in surface colour associated with bubble entrainment (Jähne & Haußecker 1998; Asher *et al.* 2002; McKenna & McGillis 2004). However, convincing parameterizations have remained elusive.

Gases such as oxygen, carbon dioxide and hydrogen sulphide (hereafter termed *constituents*) are known as sparingly soluble gases due to their low solubility in water. At low to moderate wind speeds, the central problem is defining a rate of mass exchange between the two distinct fluid masses on either side of the interface which remain well mixed by turbulence far from the surface. It is well established that the resistance to transfer across air–water interfaces is controlled by diffusion sublayers on either side of the interface in which the tiny molecular diffusivities dominate the net mass flux. For low-solubility constituents this resistance is primarily in the aqueous phase (Lewis & Whitman 1924; Jähne & Haußecker 1998). While the molecular processes controlling heat and shear-stress-related momentum exchange take place within the upper 1 mm of an unruptured water column, those molecular processes governing constituent transfer occur within so-called aqueous diffusion sublayers which are believed to have thicknesses less than 200 to 300 μm. Reliable measurements in these microscopic layers are hard to achieve.

As the turbulence immediately below the air–water interface intensifies, the rate of constituent exchange across the air–water interface also increases (Lewis & Whitman 1924; Downing & Truesdale 1955). Aqueous near-surface turbulence is primarily generated by wind shear and wave breaking (Peirson & Banner 2003). However, the generation of turbulence is concomitant with myriad other complex surface behaviours which give wind-forced open waters their great beauty (Mitsuyasu 2009).

At strong levels of wind forcing ($U_{10} > 15$ m s^{-1}, where U_{10} is the wind speed 10 m above the surface), constituent exchange may also be enhanced by other processes. These include air entrainment via more visible larger waves that break on shorelines or

as 'white caps' on open waters. Similarly, high constituent exchange can be observed in rivers and streams generated by air entrainment associated with cascades, rapids and high subsurface turbulent intensity. However, for moderately wind-forced open waters, the aerial extent of bubble entrainment is usually small in comparison to that of microscale wave activity. Other important constituent exchange processes may include rainfall, biological activity (photosynthesis and respiration) and chemical reactions.

As an initial microphysical study relevant to conditions of low to moderate wind forcing, the scope of this present contribution is restricted to wind-forced surfaces that remain intact and without droplet or bubble impact or formation. The present contribution describes a suite of strategic experiments that were designed to directly measure shear and transport immediately below wind-forced air–water interfaces, perturbed by carefully controlled gravity wave fields in a laboratory tank. Complementary bulk and microphysical measurements of re-aeration of the same tank water, after initial sparging, have been used to capture the response of the oxygen aqueous diffusion sublayer (ADS).

A review of present understanding of the potentially important microphysical processes is first presented. This is followed by a description of the facilities and measurement techniques employed during this study. The measurement results are then presented with discussion of significant systematic behaviour observed in the data, theoretical methods of adequately representing the observed behaviour and potential approaches for field application. The contribution concludes with a summary of the study findings and recommendations for future work.

2. Microphysical processes influencing constituent exchange

2.1. *Microphysics*

Characterisation of constituent exchange across air–water interfaces requires determination of the mass flux F in terms of the constituent concentrations in the well-mixed bulk of the air mass (C_A) and water mass (C_B) at some distance from the free surface. Far from the interface, turbulent mixing ensures that the bulk concentrations remain largely uniform and spatial concentration gradients remain small. As the interface is approached ($|z| \ll 1$ mm, where z is the distance normal to the interface), molecular processes become more important and significant concentration gradients can develop.

As intact fluid boundaries are approached, turbulent behaviour becomes suppressed and the behaviour of a constituent of concentration C with molecular diffusivity D is governed by the advection–diffusion equation:

$$\frac{\partial C}{\partial t} + u_i \frac{\partial C}{\partial x_i} = D\left(\frac{\partial^2 C}{\partial x_i \partial x_i}\right), \tag{2.1}$$

where t is time, and x_i are orthogonal coordinate directions nominally in the down-wind, cross-wind and surface-normal directions with respective velocity components u_i. The molecular diffusivity D may vary according to the fluid temperature and the presence of other solutes.

Within the turbulent well-mixed bulk, spatial gradients in the down- and cross-wind directions are negligible, but very close to the interface this is not the case (Woodrow & Duke 2001; Takehara & Etoh 2002).

Constituent exchanges occur concomitantly with momentum transfer (Peirson & Banner 2003; Jessup & Phadnis 2005) requiring that the velocities be determined

from the Navier–Stokes equations:

$$\frac{\partial u_j}{\partial t} + u_i \frac{\partial u_j}{\partial x_i} = g_i - \frac{1}{\rho_w}\frac{\partial p}{\partial x_j} + \nu \left(\frac{\partial^2 u_j}{\partial x_i \partial x_i} \right), \tag{2.2}$$

where g_i represents gravitational body forces in the local coordinate system, noting that the water density ρ_w and kinematic viscosity ν may also vary according to temperature and solutes present.

For intact fluid boundaries, the continuity equation provides a constraint on the orthogonal fluid velocities:

$$\frac{\partial u_i}{\partial x_i} = 0. \tag{2.3}$$

Boundary conditions far from the interface can be developed by assuming bulk values with negligible spatial gradients, but at the interface itself, the boundary conditions introduce additional complexity.

One well-established simplification is that constituent phase equilibrium is maintained at the interface at all times. The surface aqueous boundary condition for concentration can be specified as C_I which can be directly determined from the constituent solubility and the concentration on the air side of the interface using Henry's Law (Scriven & Pigford 1958). However, the presence of interfacial waves requires that surface-aligned coordinate systems may deviate significantly from the horizontal and the interaction between wind and the surface waves determines the applied interfacial normal and tangential stresses (Banner & Peirson 1998).

While exciting recent microphysical numerical studies that incorporate this array of complexity are being published (e.g. Tsai & Hung 2011), conventional approaches that incorporate major assumptions and simplifications have had considerable success, as described below.

2.2. *Stagnant film model*

At the interface itself, molecular processes are anticipated to dominate and the vertical mass flux can be determined by averaging the concentration gradient in the surface-normal direction $x_3 = z$ and the definition given by the one-dimensional form of Fick's law:

$$F = -D \left\langle \left. \frac{\partial C}{\partial z} \right|_{z=0} \right\rangle, \tag{2.4}$$

where the angle brackets denote spatial averaging.

Lewis & Whitman (1924) proposed a two-film theory in which the transfer of gases across the air–water interface is controlled by the rate of diffusion through 'surface or stagnant films' of gas and liquid adjacent to the interface. Outside these films, the separate bulks of the two media are assumed to remain well-mixed. Further, with the major resistance to constituent transfer being in the aqueous phase, they characterized the mass flux by:

$$F = -k_v \left(C_I - C_B \right), \tag{2.5}$$

where k_v is the so-called transfer or piston (scalar) velocity.

Taking the concentration gradient as constant across the ADS, (2.4) and (2.5) yield:

$$\delta_d = \frac{D}{k_v}, \tag{2.6}$$

where δ_d is the thickness of this idealized ADS.

2.3. *Boundary layer behaviour*

A fundamental assumption in the development of the two-film theory and the consequent relationship between the transfer velocity k_v and the thickness of the diffusion sublayer δ_d is that the concentration profile within the diffusion sublayer remains linear.

By neglecting any transport processes adjacent to the interface and surface-parallel spatial gradients in concentration, Deacon (1977) introduced a turbulent diffusion coefficient K_c obtained from studies of smooth solid surfaces to obtain:

$$F = -\left(D + K_c\left(z\right)\right)\frac{\mathrm{d}C}{\mathrm{d}z}. \tag{2.7}$$

Assuming a constant flux, Deacon integrated the resistance to exchange across the boundary layer and determined the enhanced mass flux due to wind as:

$$k_v = \frac{1}{12.2} Sc^{-2/3} u_*^w, \tag{2.8}$$

where the Schmidt number Sc is the ratio of constituent molecular viscosity to molecular diffusivity. The aqueous friction velocity u_*^w at the interface is determined from the mean momentum flux τ applied by the wind to the air–water interface (Donelan 1978, p. 273):

$$\tau = \rho_a (u_*^a)^2 = \rho_w (u_*^w)^2 + \frac{1}{2}\frac{\mathrm{d}E}{\mathrm{d}x}, \tag{2.9}$$

where u_*^a is the corresponding friction velocity at the air side of the interface, E is the energy density of the wave field and $x = x_1$.

Deacon (1977) used laboratory data from Hoover & Berkshire (1969) and Liss (1973) to verify his model. At wind speeds greater than 3.5 m s^{-1} ($u_*^a \cong 0.16$ m s^{-1}) and the onset of waves, Deacon's model substantially underpredicts observed flux rates. Deacon (1977) initially attributed the sudden increase in the mass flux at wind speeds greater than 3.5 m s^{-1} to the formation of capillary ripples on the water surface but later (Deacon 1981) attributed the difference to the onset of microscale breaking.

Microscale breaking waves (Banner & Phillips 1974) are a widespread feature of any clean water surface above a very low wind speed threshold and generate very high near-surface vorticity (Banner & Phillips 1974; Longuet-Higgins 1995; Toba & Kawamura 1996; Peirson & Banner 2003). Above wind speeds of approximately 5 m s^{-1}, microscale waves break (e.g. Banner & Phillips 1974) and are characterized by a confined spilling region immediately leeward of the wave crest (Peirson & Banner 2003).

At a free surface, surface-parallel velocity fluctuations are possible and a local surface divergence can be defined from (2.3) as:

$$-\left.\frac{\partial w}{\partial z}\right|_{z=0} = \left.\frac{\partial u}{\partial x}\right|_{z=0} + \left.\frac{\partial v}{\partial y}\right|_{z=0}, \tag{2.10}$$

where $y = x_2$ and $u = u_1$, $v = u_2$, $w = u_3$ and where the orthogonal coordinate directions are defined relative to the local surface.

Theoretically, using (2.10), Ledwell (1984) and Coantic (1986) determined that at a free surface:

$$k_v \propto Sc^{-1/2} \tag{2.11}$$

with McCready, Vassiliadou & Hanratty (1986) finding an identical result numerically.

McCready *et al.* (1986) also found, using a numerical model of a concentration boundary layer adjacent to a flat mobile interface, that characterization of the surface divergence may be an appropriate means of determining constituent transfer rates. They also concluded that the high-frequency velocity components contributing to the surface divergence played a primary role in determining the transfer rate.

Experimentally, Jähne *et al.* (1987) found:

$$k_v = \tfrac{1}{16} Sc^{-1/2} u_*^w. \tag{2.12}$$

The similarity in Schmidt number exponent prompted the conclusion that surface divergence plays a major role in determining the effective thickness of the ADS.

However, Jähne *et al.* (1987) also showed a transition of the Schmidt number exponent from $-2/3$ to $-1/2$ with the onset of waves. Both in the presence and absence of waves, free interfaces permit surface divergence but the fundamental reason for this transition remains unknown. This behaviour has recently been validated independently in a linear tank with a clean interface by Yan *et al.* (2011).

The Schmidt number exponent is an important aspect of air–water constituent transfer characterization. Jähne *et al.* (1987) show that extrapolation from constituent a to a second constituent b can be accomplished via:

$$\frac{k_{v,a}}{k_{v,b}} = \left(\frac{D_a}{D_b}\right)^{+n} = \left(\frac{Sc_a}{Sc_b}\right)^{-n}. \tag{2.13}$$

Consequently, when extrapolating between scalars of very different diffusivities, the value of n is crucial (Jähne & Haußecker 1998, p. 451). Between constituents, whether the Schmidt number exponent is $-2/3$ or $-1/2$ is less critical. For example, transfer rates presented for oxygen at 20 °C later can be extrapolated to CO_2 at the same temperature by multiplying by 0.91 with an accuracy of $\pm 2\,\%$ in spite of the uncertainty in n. Daniil & Gulliver (1988) compare different approaches for extrapolating transfer rates for oxygen, including relationships of the form of (2.13) and others recommended by APHA (1980), ASCE (1984).

2.4. *Surface divergence approaches*

Witting (1971) theoretically investigated the effects of plane progressive irrotational waves on thermal boundary layers. The passage of waves beneath a free surface induces surface divergence (2.10) of the ADS at time and length scales characteristic of the waves (figure 1*a*). He reported that gravity wave orbital straining can enhance the average heat flux $\bar{Q}$ by a factor of 1.38 at the maximum Stokes wave steepness ak of 0.446. The effective enhancement W was defined relative to what he termed a 'rectangular equivalent slab', essentially a volume bounded by the area of surface prior to distortion and dilation by waves, the undisturbed surface itself and a depth defined by a stagnant film (2.6):

$$W = \left[\frac{\bar{Q}_{wavysurface}}{\bar{Q}_{equiv.slab}}\right]. \tag{2.14}$$

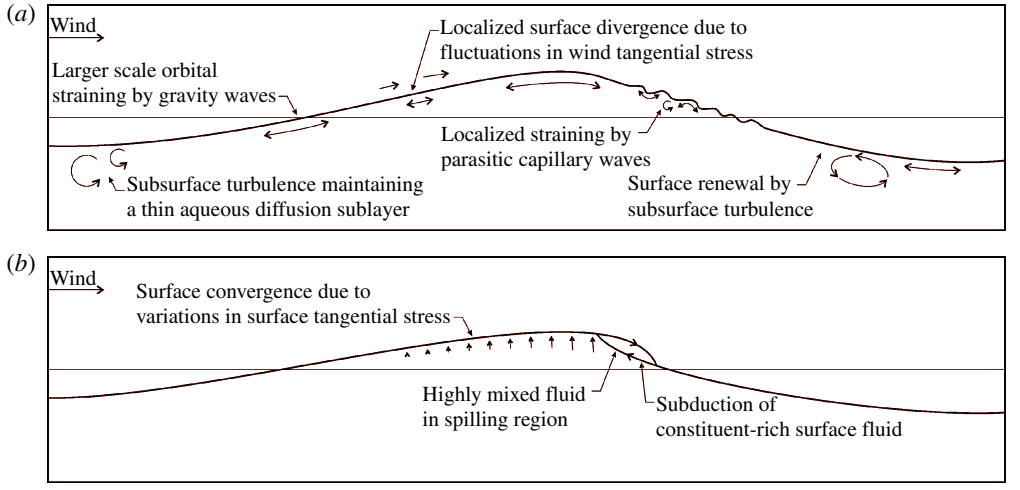

FIGURE 1. Conceptual diagrams showing those processes identified as contributing to the enhancement of constituent transfer in the presence of waves. (*a*) Steep non-breaking wave. (*b*) A small-scale breaking wave with the additional processes introduced by breaking initiation.

The enhanced flux due to the presence of waves was computed by integrating the local fluxes along the wave surface with the perturbed streamline passing through the stagnant film depth at the mean water level.

Subsequent theoretical studies by Deacon (1981), Csanady (1990) concluded that the zones of convergence and divergence due to gravity wave orbital straining are too weak to significantly influence gas transfer.

In contrast, recent experimental studies have shown good collapse of constituent transfer velocities as a function of root-mean-square surface divergence $\langle(-\partial w/\partial z)^2\rangle^{0.5}$ when the higher frequency motions are captured. Parallel studies undertaken McKenna & McGillis (2004) and Turney, Smith & Banerjee (2005) investigated constituent exchange in the presence of subsurface grid turbulence and surface wind forcing respectively. These studies characterize their results with the expression:

$$k_v = C\sqrt{D\left\langle\left(-\partial w/\partial z\right)^2\right\rangle^{0.5}} \tag{2.15}$$

to compare them with theoretical predictions (Ledwell 1984 $C = 0.64$; McCready *et al.* 1986 $C = 0.70$; Csanady 1990 $C = 0.80$; Banerjee, Lakehal & Fulgosi 2004 $C = 0.50$).

Both of these physical investigations used particle image velocimetry (PIV) techniques designed to capture the surface-parallel aqueous velocity components. Turney *et al.* (2005) demonstrate good agreement between their results and those of McKenna & McGillis (2004) when normalized in terms of the root-mean-square divergence.

2.5. *Surface renewal*

An alternative to these boundary layer models was suggested by Higbie (1935) and Danckwerts (1951) who proposed a surface renewal theory in which turbulent eddies

in the bulk of the water rise to the air–water interface and expose 'fresh surfaces' to the gaseous phase. Although the term is widely used, fluid mechanical definitions of surface renewal seem to remain vague. As discussed previously, one form of surface engulfment is wave breaking, initiated as water surface velocities near the crest exceed that of the underlying wave (Banner & Phillips 1974; Duncan *et al.* 1999; Peirson & Banner 2003; Diorio, Liu & Duncan 2009) while a second form (termed a *scar*) occurs when strong subsurface-generated turbulence ruptures the water surface (Brocchini & Peregrine 2001, p. 233).

If the surface is renewed periodically then:

$$k_v = \sqrt{\frac{D}{\pi T_e}} = \sqrt{Dr}, \tag{2.16}$$

where T_e is a time of exposure, making r an average frequency of renewal.

Komori *et al.* (1993) investigated a surface renewal parameterization for strongly wind-forced interfaces and related the frequency of turbulent eddy structures adjacent to the interface to the observed flux rates. They found:

$$k_v = 0.34\sqrt{Df_L}, \tag{2.17}$$

where f_L is the characteristic frequency of eddies adjacent to the surface.

While breaking, especially microscale breaking, is commonly observed on moderately wind-forced water surfaces, engulfment of the surface water in terms of the scars described by Brocchini & Peregrine (2001), p. 233, is not commonly observed except, perhaps, in the wakes of strongly breaking waves. For wind-forced surfaces, the mean flow, wave and turbulent energies are all concentrated immediately adjacent to the interface on the aqueous side and decline in intensity with depth (Cheung & Street 1988). If Cheung & Street's turbulent intensities are plotted in terms of associated master length scale on Brocchini & Peregrine's figure 4, the computed curves just start to intercept the turbulence rupture threshold at a tank wind speed of 9.9 m s^{-1} ($U_{10} \cong 14.5$ m s^{-1}, the wind speed calculated at a notional elevation of 10 m based on the air-side friction velocity and roughness length). Siddiqui & Loewen (2007) concluded that Cheung & Street's turbulent intensities are likely to be an overestimate for the corresponding wind conditions. Consequently, it is unlikely that scar formation will start to play a significant role until wind speeds substantially exceed this threshold.

In the subsequent discussion, reference is made to a range of observable small-scale wave features that have been proposed to play a significant role in the enhancement of air–water constituent exchange. These features are shown diagrammatically in figure 1.

2.6. *Capillary waves*

Parasitic capillary waves are a striking feature of the downwind face of steep short gravity waves (figure 1*a*) that have been the subject of extensive theoretical investigations by Longuet-Higgins (1992). He showed theoretically that steep capillary waves induce high vorticity at the crest of short gravity waves, which may potentially play an important role in constituent exchange at wind-forced water surfaces. His theoretical predictions regarding the role of parasitic capillary waves in the initiation of small-scale breaking have been verified experimentally by Qiao & Duncan (2001)

and their role in the generation of near-surface vorticity has been verified numerically by Hung & Tsai (2009).

MacIntyre (1971) showed theoretically that *localized* transfer velocities may be enhanced up to 3.5 times in the presence of capillary ripples. Szeri (1997) and Witting (1971) have also theoretically quantified constituent flux increases in the presence of capillary ripples. Saylor & Handler (1999) undertook a series of laboratory-based experiments and showed that a surface covered in capillary waves could achieve a gas flux equivalent to a wind/wave tunnel experiment with a wind of 10 m s^{-1}. However, the experiments of Saylor & Handler (1999) generate the capillaries using a vibrating table which imparts energy to the entire water column, rather than being a hydrodynamic feature localized at the air–water interface. Saylor & Handler (1999) do not seem to consider the possibility that microscale breaking may be active during their experiments but this may have been possible given their stated frequencies and wave amplitudes.

2.7. *Microscale breaking*

Csanady (1990) developed a surface vortex model to simulate the effects of microscale breaking in thinning the diffusion sublayer. He found that localized surface divergence on the windward face of the waves reduced the thickness of the diffusion sublayer and thereby made a significant contribution to gas flux enhancement. His predictions were found to be in good agreement with the observations of McKenna & McGillis (2004), although it appears unlikely that their surfaces were sufficiently strongly forced to induce microscale breaking.

Capturing the motion and shear inside the aqueous linear sublayer requires velocity measurements within the uppermost 400 μm adjacent to a rapidly moving, wavy air–water interface. Peirson (1997) developed a method of accurately measuring the motion of near neutrally buoyant particles to determine the surface velocity and tangential surface forcing of actively forced wind waves. He used long-distance microscopic visualization techniques to capture the motion of fluorescent particles with diameters between 20 and 60 μm and a relative density of 1.2.

This technique was subsequently used in a laboratory study by Banner & Peirson (1998), from which they inferred the stress partition in the wind-forced open ocean. They proposed that as the wave field develops, the wave form drag becomes increasingly prominent but the water surface remains transitionally rough at moderate levels of wind forcing. They also captured the phase modulation of the tangential stress with reference to the wave surface elevation but found it difficult to quantify the tangential stress leeward of the crest and in the wave troughs.

This work was extended by Peirson & Banner (2003) who developed a hierarchy of important surface observable convergence and divergence processes at wind-forced water surfaces. Their observations revealed regions of locally intense flow divergence on the windward faces of wind-forced waves. However, these regions of observed divergence were observed to be significantly more diffuse than the convergent zones observed at the toes of spilling regions. They determined that the mean surface drift directly induced by the wind was $(0.23 \pm 0.02)\, u_*^a$ in the trough and $(0.33 \pm 0.07)\, u_*^a$ at the crest for microscale breaking wind waves. They also observed that in a frame of reference moving with the wave, the transport in the surface layer immediately beneath the air–water interface is rearward along its entire length, except within and immediately upwind of the spilling region. In contrast to previous understanding of wind-drift surface layer flow, Peirson & Banner (2003) rarely observed transport of surface fluid forward over the crest and into the spilling region.

A complementary method of observing microscale wave breaking was pioneered by Jessup (1996) who used infrared imagery to capture breaking events on the sea surface. Jessup & Zappa (1997) were able to quantify microscale breaking using this technique which was then extended to quantify the swept area of microscale breaking and relate it to constituent exchange (Zappa, Asher & Jessup 2001). Zappa *et al.* (2004) found linear relationships between constituent transfer and the swept area of microscale breaking and, by implication, assigned a dominant role for microscale breaking in the constituent transfer process, once breaking was initiated.

A contrast can be drawn between the maximum intensity of surface divergence and convergence measured by McKenna & McGillis (2004) for their grid-stirred experiments, which was low (20 s^{-1}), and that measured by Peirson & Banner (2003) for microscale breaking waves, where the highly localized convergence rates regularly exceeded 100 s^{-1}. Turney *et al.* (2005) do not present maximum intensities of surface divergence but the scale in their figure 1 suggests values of order 15 s^{-1}. The highly localized subduction of the surface due to microscale breaking does raise questions regarding the resolution required to successfully characterize constituent exchange using surface divergence measurements. Indeed, if the toes of breaking fronts are understood in terms of moving surface fronts (Phillips 1985), near-singular values of surface divergence would be anticipated in the immediate vicinity of the toe.

Based on their PIV observations of near-surface velocity structure, Peirson & Banner (2003) predicted that the aqueous diffusion sublayer would be regularly subducted at the onset of microscale breaking. They observed intense magnitudes of vorticity (> 1000 s^{-1}) generated at the toe of the spilling regions of microscale breaking waves (figure 1*b*) and proposed that the toe of the spilling region is a point of highly localized subduction, forcing entrainment of the thin diffusion sublayer into a region of intense mixing. The intense localized subduction results in a very thin diffusion sublayer at the crest of waves that thickens with increasing residence time at the surface. As the surface fluid travels rearward relative to the wave speed, the diffusion sublayer gradually thickens as it travels along the wave windward limb, through the wave trough and finally, along the wave leeward limb before being subducted at the toe of the spilling region (figure 1). This model is therefore coupled to the wave frequency and the existence of the spilling region.

Using an order-of-magnitude analysis, Peirson & Banner (2003) estimated the transfer velocity associated with microscale breaking waves in a narrow spectral bandwidth to be:

$$k_v = (1.075 \pm 0.075) e \sqrt{pDf}, \tag{2.18}$$

where e is an efficiency factor (assumed to be 100 %), f is the wave frequency characterizing the spectral band, and p is the breaking probability. Predictions based on (2.18) showed reasonable agreement with recent bulk measurements of oxygen transfer rate under microscale breaking conditions with an efficiency of 100 % (Peirson *et al.* 2007).

2.8. *Synthesis*

Here we have reviewed the wide range of diverse observations and theoretical approaches developed over a period of at least 40 years to explain the observed strong enhancement of constituent exchange that occurs at air–water interfaces exposed to moderate winds. In figure 1, we summarize these processes graphically as they might plausibly be expected to occur along the surfaces of unbroken (figure 1*a*) waves and those additional processes that would be anticipated along the surfaces of microscale

breaking waves (figure 1*b*). The key question is: what are the relative contributions of each of these hydrodynamic features to the overall constituent flux budget?

The discussion above identifies five (probably interdependent) processes that control the thickness of the aqueous diffusion sublayer, as follows:

(i) the action and intensity of subsurface turbulence engulfing near-surface fluid elements and mixing them with the bulk; however, actual engulfment of the surface itself by turbulence is only anticipated to play a major role at strong wind speeds and not at the moderate wind speeds under investigation here;
(ii) localized surface divergence arising from turbulent motions on either side of the interface;
(iii) orbital straining of near-surface fluid elements by wave motions;
(iv) the generation of parasitic capillaries on the downwind faces of short wind waves triggering strong, localized straining and shearing of fluid elements;
(v) direct subduction of the surface by breaking, particularly at the microscale.

3. Experimental facilities and methods

A detailed description of the present laboratory investigation is presented in Walker (2009). The microphysical techniques used during the study were developed by Peirson (1997) and Walker & Peirson (2008). Preliminary findings from this investigation are described in Peirson *et al.* (2007). A compact summary of the laboratory investigation and the techniques employed is included here for completeness.

3.1. *Tank*

The wind-wave tank used for all experiments conducted in this study is linear, with an overall length of 8.955 m, width of 0.245 m and a total cavity height of 0.610 m. An electro-mechanical flexible cantilever paddle was used to generate monochromatic waves when necessary. Wind was generated by a fan fitted at the upwind end of the tank. Guide vanes downwind of the fan ensured a uniform air flow across the width of the tank and provided a smooth transition from the inlet to the water surface. Wind strength (U_{10} cm) was monitored on the tank centreline 2.4 m downwind of the inlet at an elevation of 10 cm above the still water surface. The tank is housed within a constant-temperature room and the room temperature was maintained at $21.5 \pm 0.5\,^{\circ}\mathrm{C}$ throughout these experiments.

The tank water depth varied by less than 1mm during testing with an approximate total depth of 0.247 m. The roof of the wind-wave tank is provided to achieve a zero pressure gradient along the length of the test section. The test fetch length could be adjusted by positioning of a sealed surface-skimming weir along the tank. A dissipative beach of length 430 mm and constructed of perforated steel mesh was installed at the downwind end of the fetch length to minimize wave reflections. The overall beach length remained less than 15 % of the total tank length for any test (table 1, row 2) but it was also installed to minimize the surface-pierced area of the tank (less than 5 % of the tank surface area).

Some investigators (e.g. Jähne *et al.* 1987) have used annular wind/wave tunnels to avoid variations in wave characteristics with fetch. However, a potential disadvantage of such facilities is the preferential centrifugal wave motion, the formation of secondary circulations and the promotion of stem wave breaking at the outer wall.

During these experiments, we adopted an alternative approach. By selecting appropriate fetch lengths and balancing the levels of wind forcing and wave generation against wave attenuation due to breaking and viscosity, deep-water wind-forced

https://doi.org/10.1017/jfm.2013.681 Published online by Cambridge University Press

	Experiment	F00U21AK0	F34U21AK18	F34U21AK27	F34U57AK32	F63U42AK00	F21U39AK10	F24U39AK24	F31U39AK28
1	Surface	flat water	low	incipient	microscale	ripple	low	incipient	microscale
2	Total fetch (m)	4.55	4.55	4.55	4.55	3.1	3.1	3.1	3.1
3	Water temp. (°C)	19.3	19.1	19.1	18.4	18.4	18.3	17.3	17.0
	Wind Forcing								
4	Wind speed $U_{10\ \mathrm{cm}}$ (m s^{-1})	2.1	2.1	2.1	5.7	4.2	3.9	3.9	3.9
5	u_*^a (m s^{-1})	0.12	0.13	0.22	0.52	0.18	0.24	0.32	0.42
6	z_o^a (mm)	0.009	0.020	0.140	0.330	0.002	0.023	0.164	1.03
7	τ (Pa)	0.017	0.020	0.057	0.326	0.039	0.069	0.122	0.212
8	U_{10} (m s^{-1})	4.2	4.3	6.1	13.4	6.9	7.8	8.8	9.6
	Wave Characteristics								
9	Frequency (Hz)	_	3.4	3.4	3.4	6.3 (ripples)	2.1	2.4	3.1
10	ak	0	0.18 ± 0.01	0.27 ± 0.02	0.32 ± 0.02	-	0.10 ± 0.01	0.24 ± 0.02	0.28 ± 0.02
	PIV								
11	No. of PIV observations	201		169	136			119	124
12	Sample mean u_s (m s^{-1})	0.0795		0.016	0.062			0.043	0.037
13	Sample mean τ_{tang} (Pa)	0.017±0.0013		0.014±0.002	0.037±0.015			0.045±0.009	0.046±0.011
14	Binned mean τ_{tang} (Pa)			0.014	0.033			0.044	0.045
15	Sample mean$\tau_{tang}u_{sw}/c$ (Pa)			0.0012±0.0008	0.011±0.005			0.0053±0.0019	0.0062±0.0029
16	Binned mean$\tau_{tang}u_{sw}/c$ (Pa)			0.0019	0.015			0.0069	0.0071
17	rms($-$dw/dz) (s^{-1})	13.1±22.1		35.4±21.4	168.2±331.0			56.5±102.0	69.3±106.5

TABLE 1. Summary of experiment conditions, wind-wave characteristics and PIV measurements.

wave conditions could be established for which the wave characteristics remained approximately invariant along the test length of the tank. By mechanically generating the initial wave forms, the waves maintained a constant mean frequency along the entire fetch length. Also, the mechanical generation of the wave forms enabled maintenance of approximately constant ($< \pm 10\,\%$) wave amplitudes along the entire fetch length (table 1, row 10). Thereby, significant differences in the momentum flux between either side of the interface were avoided, (2.9). The surface conditions of each of the test cases were photographically recorded and are presented in figure 2.

The presence of adventitious surfactant films on the water surface can reduce constituent transfer rates across the air–water interface and suppress the formation of microscale breaking waves (Saylor & Handler 1999; McKenna & McGillis 2004; Zappa *et al.* 2004). Considerable care was exercised to ensure that all experiments were conducted with a slick-free, clean water surface, as described below.

To minimize biological growth and eliminate surface contaminants when testing was not in progress, the water was recirculated via a pump through a diatomaceous earth filter and a UV sterilizer discharging to the upwind end of the tank test section. Water recirculating through the test chamber discharged over an overflow weir to the downstream (unused) portion of the tank where any surface contamination was trapped. During recirculation, a light wind was applied to ensure that any surface material was transported over the overflow weir. Our microscopic observations of the free surface (described subsequently) were used to confirm that there was no surface contamination present during the experiments.

3.2. *Bulk measurements*

Three capacitance wave probes based on the design of Clymo & Gregory (1975) were used to monitor wave conditions at the measurement section and at the upwind and downwind ends of the tank. Wave conditions were recorded at 1000 Hz per channel using a data acquisition system consisting of an analogue-to-digital converter (Eagle Technology, model USB26 μDAQ) fitted to a laptop computer.

The wind friction velocity u_*^a and the air roughness length z_0^a were derived from the logarithmic portions of the air velocity profiles (Kawamura *et al.* 1981) measured using a 2 mm diameter Pitot tube mounted on a Vernier scale rule on the top of the wind-wave tank and referenced to the still water level. The Pitot tube pressures were recorded using an MKS Baratron transducer (model 223BD) with a range of 0.2 Torr and recorded by the data acquisition system.

The constituent exchange experiments were undertaken by re-aeration using oxygen as the tracer. Initial oxygen depletion was achieved by nitrogen sparging via perforated 13 mm polypropylene pipes affixed to the base of the flume. Prior to each tracer experiment, nitrogen was bubbled through the water until the dissolved oxygen concentration was reduced to approximately 0.7 mg l^{-1}.

Bulk dissolved oxygen levels in the wind-wave tank were measured using an Orion model 835A dissolved oxygen meter with data logged to a computer at 5 s intervals. The dissolved oxygen probe was calibrated in accordance with the manufacturer's specifications and was shown to respond linearly over the required measurement range. In order to ensure that a sufficient water flow was maintained across the dissolved oxygen probe membrane, the probe was housed within a glass flow-cell immersed at a depth of 150 mm and water circulated past the cell by a peristaltic pump.

Following Wolff & Hanratty (1994), the transfer velocity k_{vbulk} for each experiment was obtained from the bulk dissolved oxygen measurements via:

$$\ln \frac{C_I - C(t)}{C_I - C(0)} = \frac{k_{vbulk}}{\mathrm{d}} t, \tag{3.1}$$

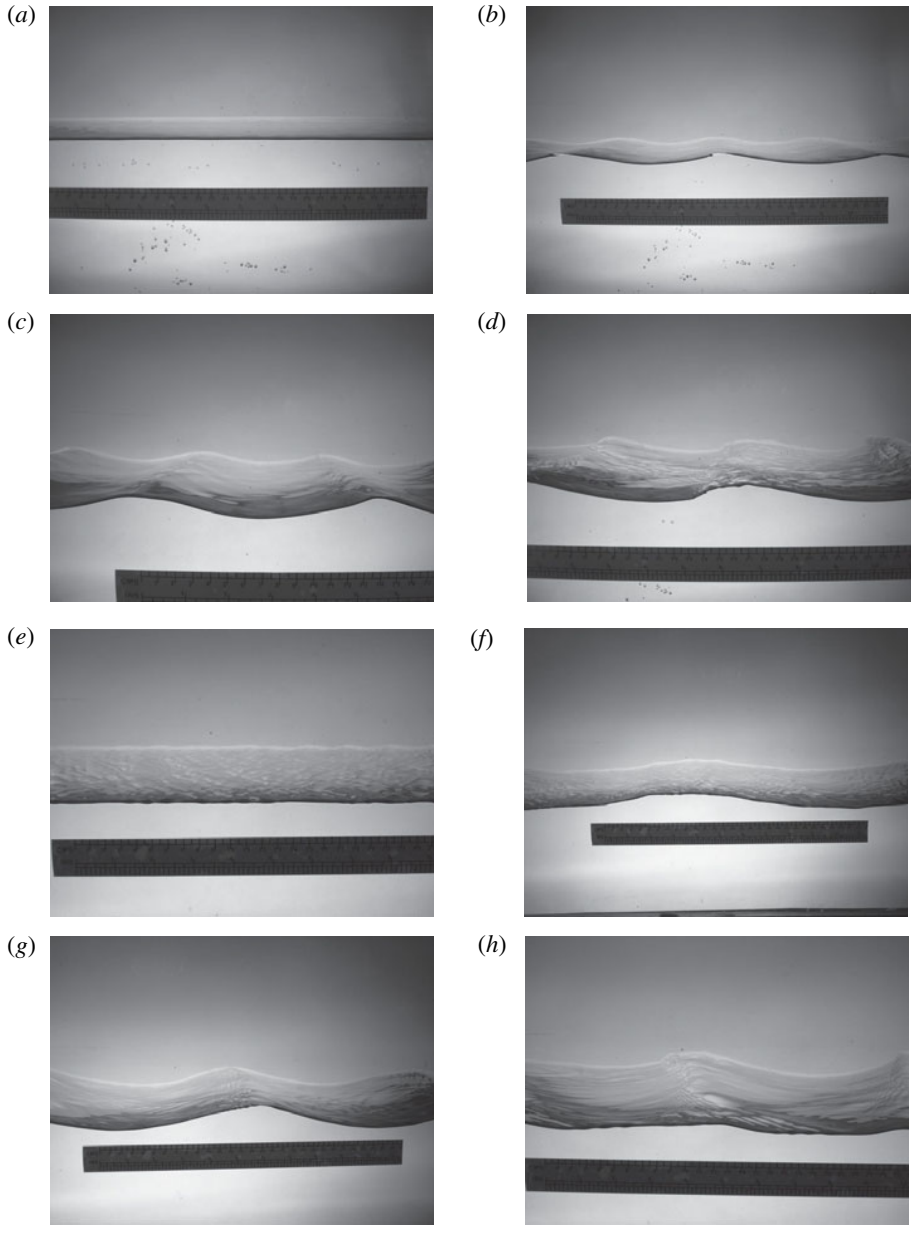

FIGURE 2. (*a*) Experiment 1 (F00U21AK0), flat water condition, wind speed 2.1 m s^{-1}. (*b*) Experiment 2 (F34U21AK18), low wave condition, wind speed 2.1 m s^{-1}, $ak = 0.18$. (*c*) Experiment 3 (F34U21AK27), incipient breaking condition, wind speed 2.1 m s^{-1}, $ak = 0.27$. (*d*) Experiment 4 (F34U57AK32), microscale breaking condition, wind speed 5.7 m s^{-1}, $ak = 0.32$. (*e*) Experiment 5 (F63U42AK00), ripple condition, wind speed 4.2 m s^{-1}. (*f*) Experiment 6 (F21U39AK10), low wave condition, wind speed 3.9 m s^{-1}, $ak = 0.10$. (*g*) Experiment 7 (F24U39AK24), incipient breaking condition, wind speed 3.9 m s^{-1}, $ak = 0.24$. (*h*) Experiment 8 (F31U39AK28), microscale breaking condition, wind speed 3.9 m s^{-1}, $ak = 0.28$. In each case the wind is from the right. The scales show centimetres at the top edge and inches at the lower edge.

where: C_I is the saturation dissolved oxygen concentration on the aqueous side of the interface, $C(t)$is the bulk dissolved oxygen concentration at time t, $C(0)$ is the bulk dissolved oxygen concentration at $t = 0$, and d is the water depth in the wind-wave tank.

To minimize thermal gradients within the wind-wave tank, the sidewalls of the tank were insulated with polystyrene blocks. During the course of these experiments it was noted that the water temperature in the wind-wave tank (table 1) systematically decreased by up to 4 °C depending on the strength of the wind and wave action. To our knowledge, systematic cooling of the water has not been reported in previous gas transfer experiments but changing temperatures during the course of constituent experiments will impact on the physical and chemical properties of water. Nitrogen sparging and the constituent exchange experiments only commenced during this present study once a steady temperature in the tank was achieved after application of wind and wave forcing.

Measurements of the thermal skin temperature were made using a Horiba infrared sensor once equilibrium temperature was achieved. Each measurement showed values within 0.1 °C of the bulk temperature recorded by the dissolved oxygen probe and no systematic difference in thermal skin behaviour could be observed.

3.3. *PIV image capture and processing techniques*

Microscopic PIV adjacent to the moving water surfaces was undertaken at a fetch of 2.4 m using the techniques developed by Peirson (1997). A brief summary of the equipment and methods used follows below.

The digital camera selected for all PIV and LIF (laser-induced fluorescence) imagery was a Santa Barbara Instrument Group (SBIG) ST-10XME Charged Coupled Device (CCD detector KAF3200ME) with 2184 horizontal pixels × 1472 vertical pixels, read noise of 11e- r.m.s. and full well capacity of 77ke-). The SBIG camera has high quantum efficiency in the UV spectral range (50–60 %) and was also suitable for the PIV imagery. For the LIF imagery, discussed below, dark current and random readout noise were minimized by regulated cooling to −10 °C and double-correlated sampling. The camera was fitted with extension bellows and a Nikon ED 80 to 200 mm focal length lens (with a maximum operational aperture setting of f/4) to yield pixel measurement resolution of 4.15 μm *in situ*.

The PIV illumination was a 6W water-cooled argon ion laser modulated by an electromechanically driven precision wheel generating four light pulses at a frequency of approximately 500 Hz. The fourth pulse generated is of lower intensity to indicate particle direction. The laser illumination was directed through the floor of the tank in a light sheet with its plane parallel with the walls of the tank. The physical configuration of the PIV system is as shown in figure 3(*a*). Peirson (1997) used *Dayglo ZQ-17* particles which have a characteristic relative density of approximately 1.2. For this investigation, we used *Pliolite VT-AC-L*, a white material with a relative density of 1.03. The particles were milled to achieve a size distribution with $D_{20} = 12$ μm and $D_{80} = 50$ μm (Walker 2009). *Pliolite* has very good light scattering properties and particles remained in suspension for several weeks without agitation.

The camera was mounted with its optical axis at +8° above the horizontal (figure 3) so that the viscous sublayer immediately adjacent to the water surface could be observed clearly in spite of variations in cross-tank surface slope or position of the sidewall meniscus. A wave probe was mounted immediately downwind of the imaged area to measure water surface elevation and synchronize wave phase with the light sheet and the camera shutter.

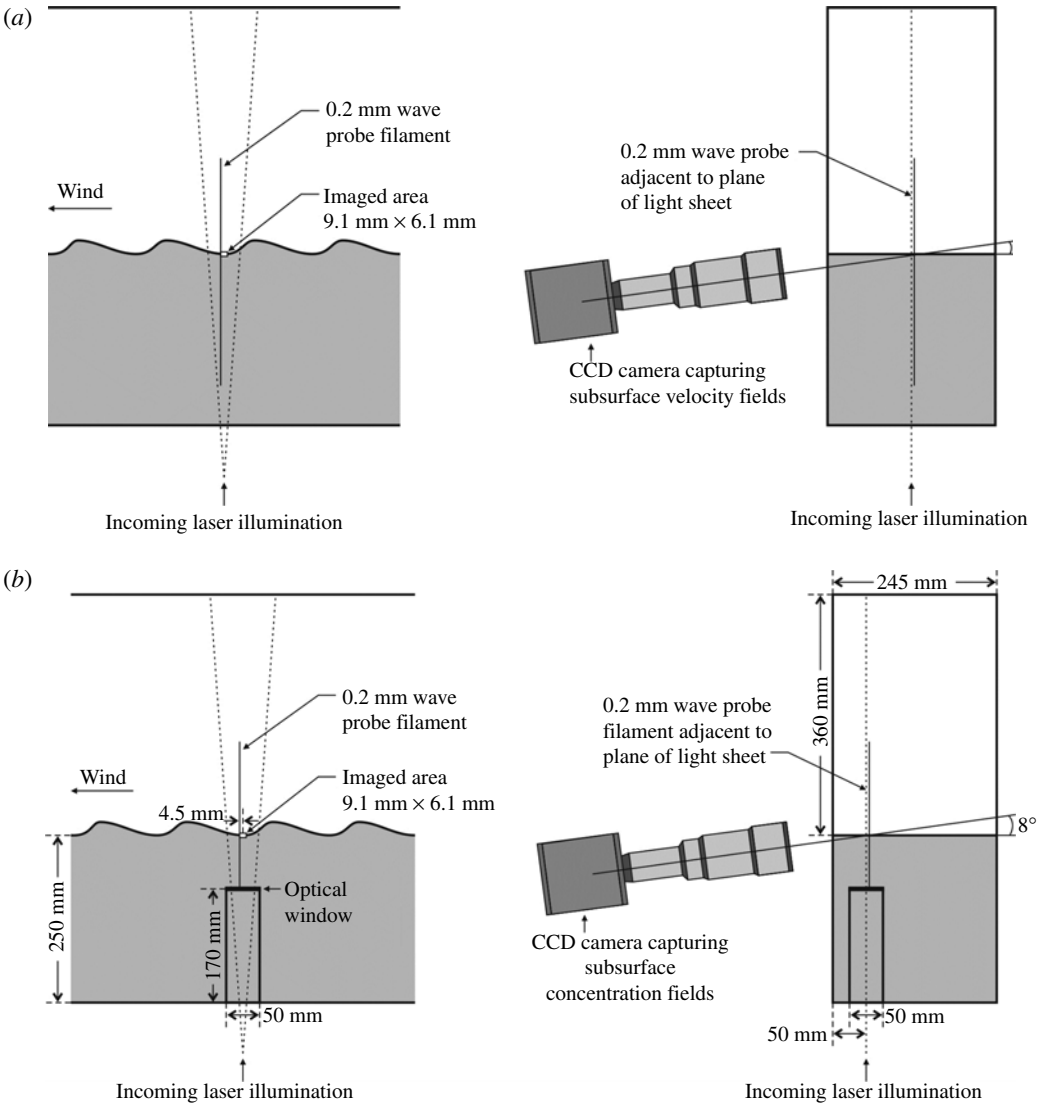

FIGURE 3. (*a*) Light sheet, camera and wave probe configuration during the particle image velocimetry (PIV) experiments. (*b*) Configuration during the laser-induced fluorescence (LIF) experiments.

By processing images captured at approximately 2 s intervals during the passage of the freely propagating waves to detect the motion of adjacent particle pairs, the surface viscous stress and surface velocity could be determined. Peirson (1997, p. 432*ff*), provides a detailed description of the local surface conditions for which reliable measurements cannot be obtained and processing of the particle images is painstaking. For reliable measurements, it was essential that each particle processed also have a clearly recognizable reflection in the water surface to determine the water surface position and the particle depth accurately (± 4.15 μm for this present experimental condition). The total system errors generated a total velocity error of less than 5 % for near-surface velocities of 0.1 m s^{-1}.

Banner & Peirson (1998, p. 124) assumed at the interface

$$\tau_{visc} = \mu \left. \frac{\partial u}{\partial z} \right|_{z=0}, \tag{3.2}$$

where τ_{visc} is the local surface-parallel tangential stress, u is the velocity component parallel to the surface, μ is the absolute viscosity of water and z is the surface-normal direction. Subsequent review of Longuet-Higgins (1953) showed that (3.2) neglects a vorticity contribution due to the surface motion. Our measurements under conditions of weak surface forcing indicated that there was a systematic, phase-related error in (3.2). Re-writing equation (197) in Longuet-Higgins (1953) in terms of surface velocities and the present notation gives

$$\tau_{visc} = \mu \frac{\partial q_s}{\partial z} - \kappa q_s, \tag{3.3}$$

where q_s is the velocity component parallel to the surface in a frame of reference moving with the waves and κ is the surface curvature. The practical implication of this difference is that using (3.1) will underestimate the tangential stress at the wave crests and overestimate it in the wave troughs.

While q_s is readily obtained from the PIV measurements (Banner & Peirson 1998), measuring κ along the surfaces of rapidly moving waves with digital imagery is a challenging task. Further, κ depends on a second derivative in space, and the error in finite difference estimates increases with the square of the reciprocal of the spatial resolution. Our present solution to this problem was to derive the surface curvature as a function of phase based on a fifth-order Stokes approximation to the wave surface profile. As shown in panels (*a*) of figures 4–7, this provided a reasonable approximation except immediately adjacent to the spilling region of microscale breaking waves. However, reference to figure 2 indicates that the transit of surface ripples also has the potential to cause fluctuations in the local surface curvature. During this present study we were unable to resolve this issue but the recent high-resolution spatial measurements along the surface of breaking waves completed by Diorio *et al.* (2009) shows that it should be possible to address this issue in the future. In this present assessment, the mean phase-averaged bias introduced by neglecting curvature-related vorticity is zero, with the highest local deviation occurring at wave crests with a maximum value of 0.015 Pa if the fifth-order Stokes forms are assumed.

The viscous stress contributions to the horizontal momentum flux and wave growth were computed as summarized in Peirson & Garcia (2008, p. 246). The wave-coherent tangential stress was computed in an identical manner to that used by Banner & Peirson (1998).

In addition to quantifying the surface tangential stress, the surface divergence may play a significant role in constituent exchange. The surface divergence was readily obtained from the near-surface PIV data by evaluating the quantity $\partial w/\partial z|_{z=0}$ (see (2.10)).

3.4. *LIF image capture and processing techniques*

Laser-induced fluorescence (LIF) measurements were undertaken using the techniques developed by Walker & Peirson (2008) at the same location and using the same imaging camera and lens configuration as used for the PIV measurements.

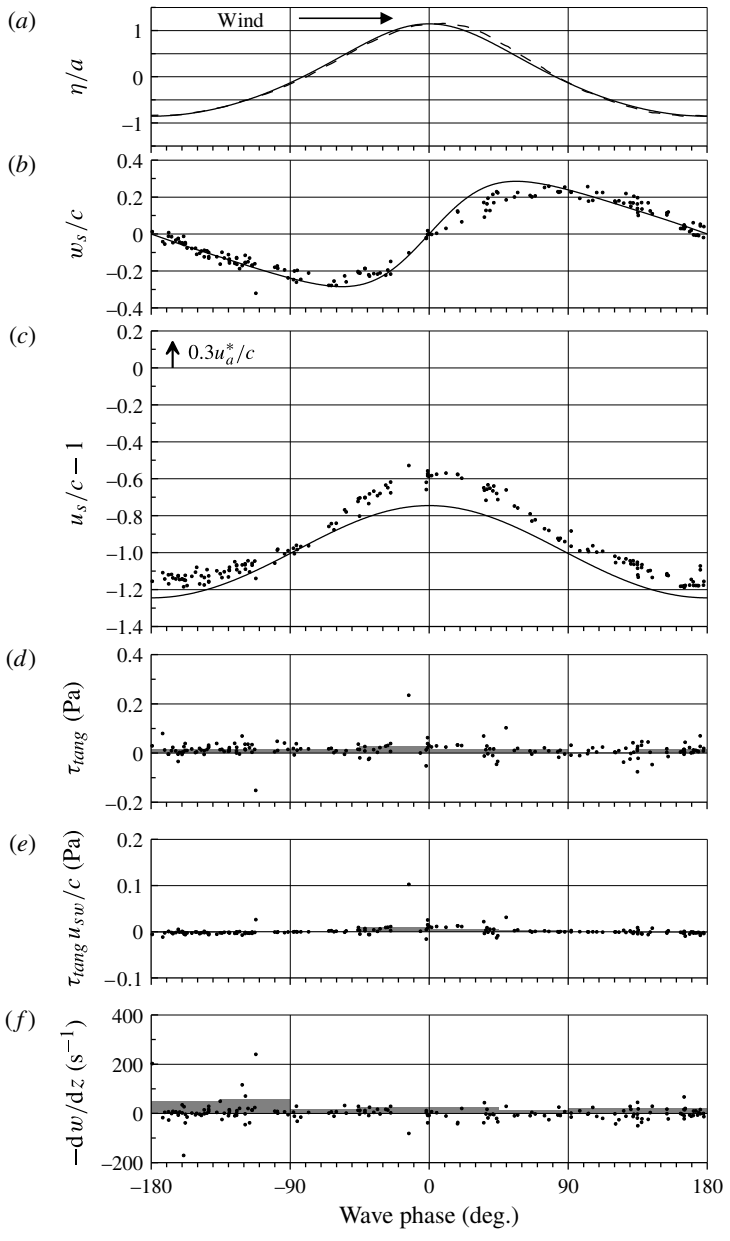

FIGURE 4. PIV surface data for experiment F34U21AK27 (incipient breaking). (*a*) A representative wave profile (dashed curve) with the corresponding fifth-order Stokes profile (solid curve). (*b*) Vertical velocity component normalized by the wave speed (points) with the fifth-order Stokes estimate (solid curve). (*c*) Horizontal velocity normalized by wave speed in a frame of reference moving with the wave (points) and fifth-order Stokes estimate (solid curve). (*d*) Surface tangential stress, instantaneous values shown as points with 45° bin averages shown as solid bars. (*e*) Wave coherent tangential stress, instantaneous values shown as points with 45° bin averages shown as solid bars. (*f*) Surface divergence, instantaneous values shown as points with 45° bin averages shown as solid bars.

With Schmidt numbers for oxygen of approximately 550, the ADS is approximately an order of magnitude smaller than the viscous sublayer (Deacon 1977, figure 1). Consequently, reliable LIF measurements within the diffusion sublayer are even more challenging than PIV measurements in the viscous sublayer.

The LIF procedures employed during these experiments are described in detail in Walker & Peirson (2008) and were developed for practical application to strongly forced laboratory conditions by extending the techniques originally developed by Wolff & Hanratty (1994) and Woodrow & Duke (2001). Parallel techniques employing HCl and CO_2 have been developed by Münsterer & Jähne (1998) and Takehara & Etoh (2002) respectively.

The objective was to directly observe and quantify oxygen profiles within the aqueous diffusion sublayer. This is achieved by LIF imagery of collisional oxygen quenching of dissolved pyrenebutyric acid (PBA) appropriately illuminated by a pulsed UV laser light sheet. As oxygen concentrations are reduced, there is less collisional quenching and more energy emitted by the PBA molecules stimulated by UV irradiation. The fluorescence emission can be captured with a suitable digital camera system.

For this present study, LIF illumination was provided by a PTI model GL3300 nitrogen laser (wavelength 337.1 nm, pulse width of 600 ps). Optical materials must be carefully chosen to minimize losses during UV light transmission. A series of UV fused silica lenses and suitable mirrors were used to focus the light sheet to approximately 6 mm wide $\times$ 0.4 mm thick at a distance of 985 mm from the laser and at a point where the light sheet vertically intersected the water surface. The fluorescence within the generated light sheet was observed through a 50 mm diameter UV silica window fitted to the sidewall of the wind-wave tank. Between the Nikon lens and the CCD camera a low-pass edge filter ($< 1\,\%$ transmission for wavelengths < 340 nm) was added to minimize scattered incident laser light.

There are two major challenges for such investigations:

(i) Attenuation of the incident and emitted light within the PBA-dosed water is a compromise between absorbance and fluorescence. By judicious selection of geometry and PBA concentration (0.0272 mg l^{-1}) coupled with appropriate corrections for Lambert–Beers decay, implementation of the Stern–Volmer relationship and adjustment for modulation in the incident laser illumination, an instantaneous measurement of oxygen concentration could be made with an accuracy of ± 0.15 mg l^{-1}. To ensure that images with sufficient intensity could be captured by the imaging camera, the LIF light sheet plane had to be displaced 72.5 mm towards the imaging camera from the position of the PIV light sheet. To avoid unnecessary attenuation of the UV light within the tank, a 50 mm diameter by 170 mm long light tube capped with a UV silica window was mounted vertically within the tank to carry the UV light through the bulk of the water column (figure 3*b*).

(ii) Oblique imagery of a fluorescing light sheet of finite width with nonlinear variation in emission intensity will lead to optical blurring. Walker & Peirson (2008) carefully assessed optical blurring of concentration profiles in the vicinity of the free surface and determined the influence of view angle, light sheet thickness and aeration rate on the measured results.

The optical properties of the camera/lens system can be sensitive to the illuminating light frequency. Specifically, the use of complex lens systems under UV light can yield significant levels of optical diffraction that are not present under visual light. This

potential problem was not identified during the study because imagery obtained using the UV light source during geometric system set-up did not indicate any noticeable increase in optical diffraction. Subsequent analysis of physical scales captured within the original imagery showed negligible influence of optical diffraction on the results.

The optimized measurement system consisted of two phases: image capture and image processing.

A wave probe was mounted in the wind-wave tank adjacent to the UV laser sheet and its signal was monitored in real time to generate the necessary trigger for image capture and laser discharge at specified wave phase points. Immediately after capture, the images were downloaded to a host computer for subsequent processing. The original wave probe data with the instant of laser discharge was also stored for subsequent determination of precise image wave phase.

Image processing was automated using a number of user-defined Fortran subroutines. However, the data were carefully monitored for quality by visually checking the original images to ensure that any extreme values determined by the image processing process accurately represented the original captured imagery. The key data processing steps were as follows:

(i) An approximately 0.8 mm wide strip captured from 202 adjacent image columns was extracted from each image with the region of highest uniform illumination and smoothed with a 3×3 box-car smoothing filter reducing the data file width to 200 columns.

(ii) The air–water interface was identified by detecting the row with the minimum intensity in each data column: fitting a linear equation to the row and column numbers and retaining data that yielded fits with a correlation coefficient greater than 0.9.

(iii) The fluorescent signal image was converted to a dissolved oxygen concentration profile using image scale, the Lambert–Beers decay relationship and the Stern–Volmer equation.

(iv) Data contaminated by surface optical blurring (on average contained in a layer within 28 μm of the interface) were eliminated by detecting the depth of maximum dissolved oxygen concentration gradient and removing data between this depth and the surface.

(v) The surface oxygen concentration gradient, flux and transfer velocity were determined from an error function fitted between a saturated value at the interface and the point of measured maximum oxygen concentration gradient.

Our reasoning for selecting the error function profile was as follows. Scriven & Pigford (1958) showed that the saturation concentration must exist at the surface. Linear extrapolation of the maximum concentration gradient to the surface yielded concentrations at the surface that were consistently less than the saturation concentration (see also Woodrow & Duke 2001). The error function profile was selected because it is the solution to Fick's law (see (2.4)) for unsteady re-aeration of an aqueous medium of initially uniform concentration C_B with aqueous interfacial concentration C_I, the solution of which yields

$$\frac{C_I - C(t, z)}{C_I - C_B} = \mathrm{erf}\left(\frac{z}{2\sqrt{Dt}}\right). \tag{3.4}$$

Walker & Peirson (2008) show that this approach is a significant improvement on previously developed applications and plausibly reconciles the highly localized LIF measurements of constituent flux with the fluxes determined from bulk measurements.

3.5. *Wind-wave conditions*

Mechanically generated waves were selected for this present investigation to minimize the group modulation effects of pure wind-generated waves and therefore accentuate the contrast between the incipient breaking and continuously breaking condition. This approach has a substantial track record (Banner 1990). The breaking statistics of mechanically generated and pure wind waves can differ substantially for short fetches.

A total of eight wind-wave cases were investigated, judiciously selected to capture representative and significant transitions in small-scale wave behaviour. When initiated in our wind-wave tank, these cases were observed to maintain approximately uniform surface wave behaviour along the entire test fetch length. The primary process responsible for slight fetch dependence in the surface conditions was the tendency of the initially monochromatic wave trains to degenerate into wave groups.

The defining parameters for each experiment, including wind strength, wave forcing and bulk aeration rate are presented in table 1. LIF measurements were undertaken for all eight cases but because of the time required to undertake detailed measurements, the project duration only permitted PIV measurements to be completed for five experiments, selected to capture behaviour in the absence of waves and the transition from incipient breaking to continuous microscale breaking.

Photographs of the water surface for each of the eight wind-wave experiments are presented in figure 2. Several water surface descriptors are subsequently used and are defined as follows:

(i) A *flat water* condition which appears free of any freely propagating wave motion but with evidence of high-frequency vertical oscillation due to pressure fluctuations in the applied wind. Case 1 was undertaken at the maximum wind speed that could be sustained without wave formation (figure 2*a*).

(ii) A *ripple* condition for which the water surface is covered with vigorous high-frequency, freely propagating capillary ripples. The ripples are approximately 2.5 mm in height (figure 2*e*)

(iii) A *low wave* condition in which the gravity waves maintain lengths between 135 and 350 mm and a low wave steepness with no evidence of parasitic capillaries (figure 2*b*,*f*).

(iv) An *incipient breaking* mode in which the waves are as steep as possible without lapsing into a microscale breaking state. These waves are accompanied by well-developed parasitic capillaries leeward (forward) of the wave crests (figure 2*c*,*g*). Careful point visual observations over several minutes showed that these waves were never observed to lapse into a microscale breaking state (and therefore the breaking probability was 0 %).

(v) Continuous *microscale breaking* in which a confined spilling region is evident immediately leeward of the wave crest, trailing subsurface turbulence with attendant capillaries downwind. The presence of parasitic capillary waves and microscale spilling leeward of the crest is evident in figure 2(*d*,*h*). Visual observations over several minutes showed that each wave appeared to maintain a continuous microscale breaking state (and therefore the breaking probability was determined to be 100 %).

Each experiment has been designated by the intrinsic wave frequency, wind speed and characteristic wave steepness, for example, experiment F34U21AK18 signifies a wave frequency of 3.4 Hz, a wind speed of 2.1 m s^{-1}, and a wave steepness of 0.18. The experiments proceeded in two stages: the first three experiments were undertaken

with a constant wind speed of 2.1 m s^{-1} without the surface conditions changing significantly with fetch. However, for the fourth experiment, the waves that were initially paddle-forced into a microscale breaking state lapsed into a non-breaking state as they propagated along the tank with a wind speed of 2.1 m s^{-1}. It was necessary to increase the wind forcing to 5.7 m s^{-1} to maintain microscale breaking along the full fetch length.

The significant increase in forcing by wind speed was undesirable as the objective was to change the surface condition while maintaining a similar level of wind forcing. Consequently, the second epoch of experiments was developed by establishing that a similar forcing wind speed and approximate laboratory fetch independence of the surface wave conditions could be maintained by slightly reducing the tank length and decreasing the wave frequency (table 1, rows 2 and 9).

The variation in wave characteristics along the entire fetch is indicated in table 1 by the variation in ak and in all cases remained less than 10 % of the local value at the point where the microphysical observations were undertaken.

4. Results and discussion

4.1. *PIV results*

Detailed PIV measurements were obtained for five of the eight wind-wave experiments, namely: the *flat water* case, the two *incipient breaking* cases and the two *microscale breaking* wave cases. The numbers of PIV measurements and the statistics of the processed data for each case are summarized in rows 11 to 17 of table 1.

Within any given PIV image the spatial position of each illuminated particle is captured at four instants approximately 2 ms apart. For each particle so captured, velocities were measured between proximate pairs of images of a given particle and averaged to obtain a mean velocity for the total duration of particle observation (Peirson 1997). Potentially, these data could be reprocessed to obtain particle accelerations but this has not been undertaken to date.

For the *flat water* case, a mean surface velocity of 0.0795 m s^{-1} was measured (table 1). Given that freely propagating waves are absent from the surface, the mean surface velocity is the surface drift formed directly from wind-induced skin friction. The mean surface drift $\langle u_s \rangle / u_*^a = 0.66$ is approximately 20 % greater than that measured by Banner & Peirson (1998) for a much shorter fetch (0.13 m) but with stronger wind forcing. The standard deviation of the surface drift is $(u_s)/u_*^a = 0.12$ and highlights the mobile nature of the surface.

The processed PIV data captured for the *incipient* and *microscale breaking* wave cases are summarized in figures 4–7 as a function of wave phase.

The phase location of each velocity measurement is determined relative to the immediate upwind and downwind wave crests as described previously. In each panel (*a*) of figures 4–7, a selected representative wave profile is presented in comparison with the theoretical fifth-order Stokes estimate (Skjelbreia & Hendrickson 1961). As anticipated, the actively wind-forced waves are slightly asymmetric, with the leeward faces of the waves generally steeper than the windward faces. Consequently, the wave trough may not be located precisely midway between the wave crests and there can be a consequent apparent misalignment of the calculated wave phase by up to $\pm 10^\circ$ for the *microscale breaking* wave cases.

The velocity components relative to the mean surface have been separately computed and are presented in comparison with fifth-order Stokes estimates in panels (*b*) and (*c*) in figures 4–7. For the *incipient* and *microscale breaking* cases,

the fifth-order theory estimates provide a useful theoretical reference for comparison with the measured data. The scatter about the mean increases systematically as a function of wind speed and transition from an incipient to microscale breaking state. Any scatter due to modulations in the wave fields is minor as the standard deviation in wave amplitude for these steeper wave cases remains less than 10 % (table 1, row 10)

In the case of the horizontal component, the movement of surface fluid relative to the wave forms is of key interest. Consequently, in figures 4–7 panels (*c*) the horizontal velocity components have been normalized relative to the propagating wave form using the linear gravity theoretical wave speed. Nonlinearity in the wave propagation speed of the wave forms and an underlying drift current can increase the wave speed relative to a fixed location. In an almost identical tank and at a similar fetch, Peirson & Banner (2003) found that the difference between the measured wave speed and the theoretical estimate was less than 10 %. By quantifying monochromatic wave frequency just downwind of the paddle and at the PIV measurement point, the surface drift velocity of the wave forms in this present study was less than 1 % of the linear wave speeds and inconsequential to the conclusions of this study. The solid lines in each of the plots represent the theoretical fifth-order Stokes estimate (Skjelbreia & Hendrickson 1961).

The Stokes estimates of the horizontal velocity data form a natural approximate lower bound to the measurements, consistent with the findings of Peirson & Banner (2003). Similar to the vertical velocity data, the variability in the surface velocities increases when the friction velocity is increased and transition to microscale breaking occurs. The mean wind-induced surface drift obtained during these experiments (panels (*c*) in figures 4–7) was $0.19 \pm 0.05u_*^a$ in the wave troughs, increasing to $0.32 \pm 0.06u_*^a$ at the crests.

Peirson & Banner (2003) observed cases in which strong injections of turbulence adjacent to the surface occurred in the presence of microscale breaking but there was also a potentially strong contribution to the variability in the surface velocities from the modulations in the wave groups within their purely wind-forced wave fields. These present measurements indicate the relative importance of the roles of the direct action of the modulations in tangential stress in comparison to the onset of microscale breaking. Following the onset of microscale breaking, comparing panels (*b*) and (*c*) in figures 6 and 7 indicates that an approximately 50 % enhancement in surface velocity fluctuations occurs in the vicinity of the wave crests. However, figures 4 and 5 highlight the dominant role of the wind stress in generating these fluctuating velocities. The standard deviations of the fluctuations about the mean are approximately equal to the magnitude of the local mean value.

A consequence of these results is that transport in the aqueous surface layer is consistently rearward along the entire wavelength in a frame of reference travelling with the wave. The exception to this is the strongly wind-forced microscale breaking case (F34U57AK32, figure 5) for which the measured surface velocities in the vicinity of the wave crests suggest that surface water speeds exceed the wave speed for a limited proportion of the time. Although the observed waves for case F31U39AK28 (figure 2*h*) certainly appeared visually to be continuously microscale breaking, the fluid actually travelling at or exceeding the wave speed must be extremely compact or transitory (see Qiao & Duncan 2001, for non-wind-forced transitions at larger scale). The present results only support the existence of an extensive roller (Csanady 1990) in the case of very strongly wind-forced waves.

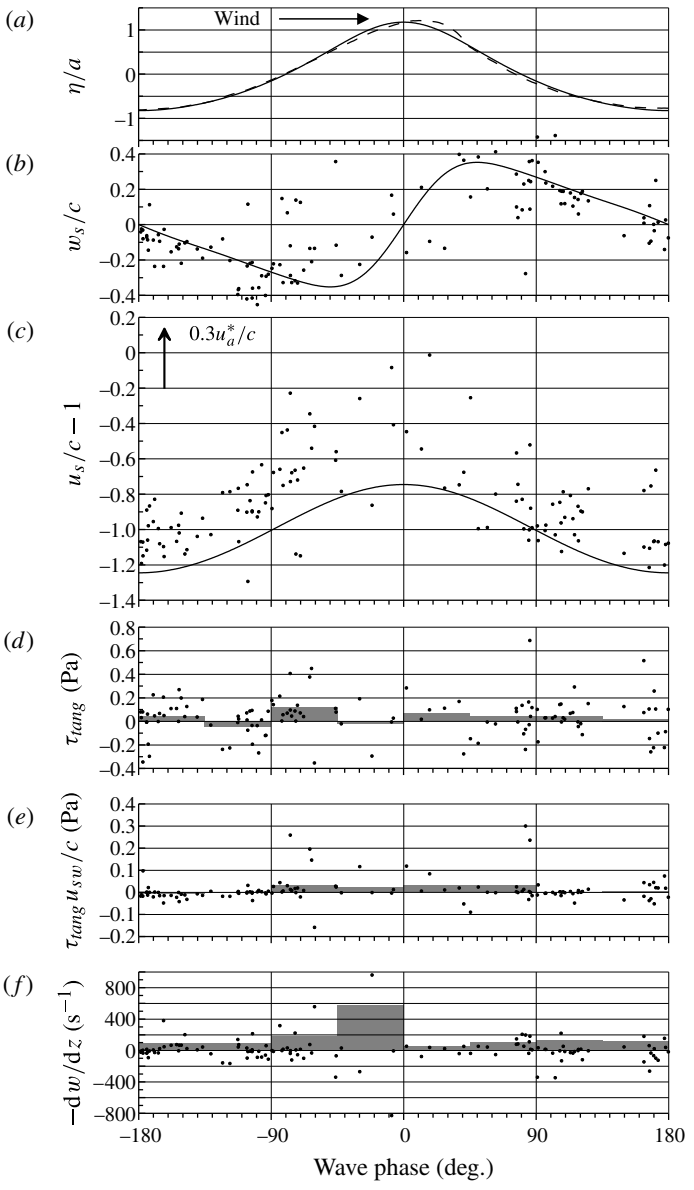

FIGURE 5. PIV surface data for experiment F34U57AK32 (microscale breaking). (*a*) A representative wave profile (dashed curve) with the corresponding fifth-order Stokes profile (solid curve). (*b*) Vertical velocity component normalized by the wave speed (points) with the fifth-order Stokes estimate (solid curve). (*c*) Horizontal velocity normalized by wave speed in a frame of reference moving with the wave (points) and fifth-order Stokes estimate (solid curve). (*d*) Surface tangential stress, instantaneous values shown as points with 45° bin averages shown as solid bars. (*e*) Wave coherent tangential stress, instantaneous values shown as points with 45° bin averages shown as solid bars. (*f*) Surface divergence, instantaneous values shown as points with 45° bin averages shown as solid bars.

4.1.1. *Tangential stress*

Panels (*d*) of figures 4–7 present the tangential stress data processed as described in § 3. In table 1, the mean tangential stress is estimated by two methods: row 13 shows

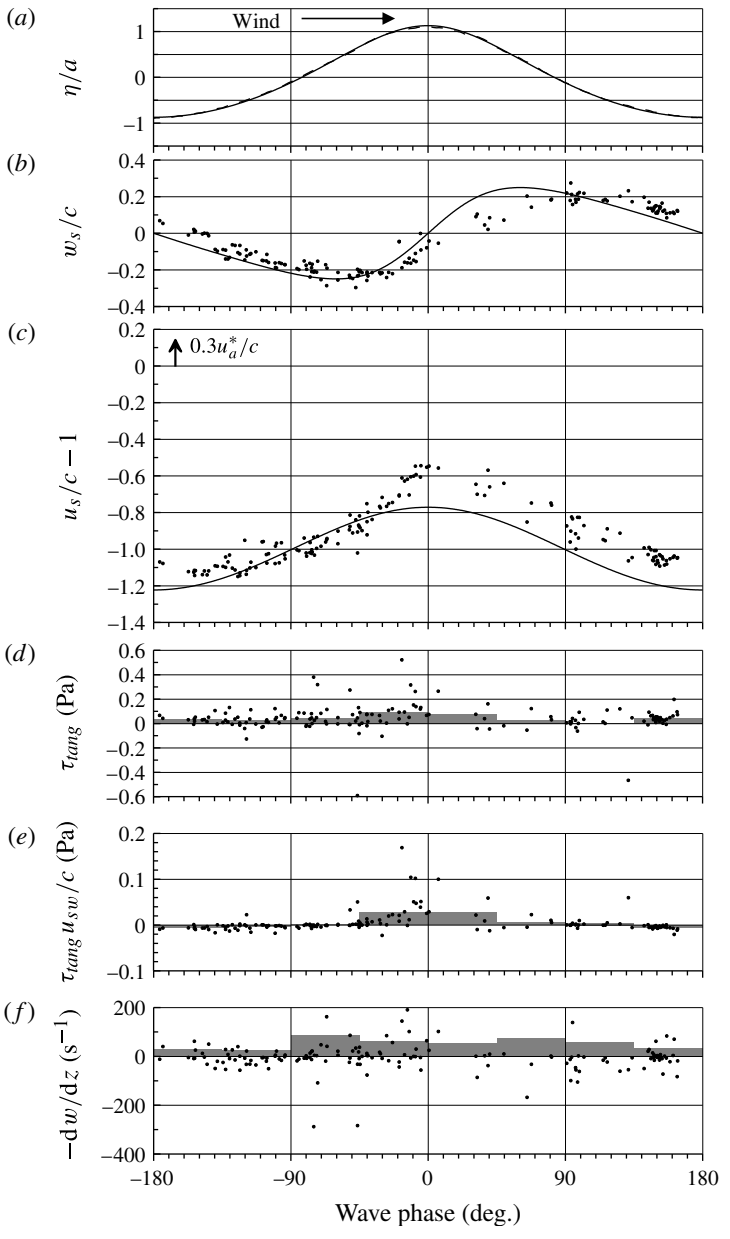

FIGURE 6. PIV surface data for experiment F24U39AK24 (Incipient breaking). (*a*) A representative wave profile (dashed curve) with the corresponding fifth-Stokes profile (solid curve). (*b*) Vertical velocity component normalized by the wave speed (points) with the fifth-order Stokes estimate (solid curve). (*c*) Horizontal velocity normalized by wave speed in a frame of reference moving with the wave (points) and fifth-order Stokes estimate (solid curve). (*d*) Surface tangential stress, instantaneous values shown as points with 45° bin averages shown as solid bars. (*e*) Wave coherent tangential stress, instantaneous values shown as points with 45° bin averages shown as solid bars. (*f*) Surface divergence, instantaneous values shown as points with 45° bin averages shown as solid bars.

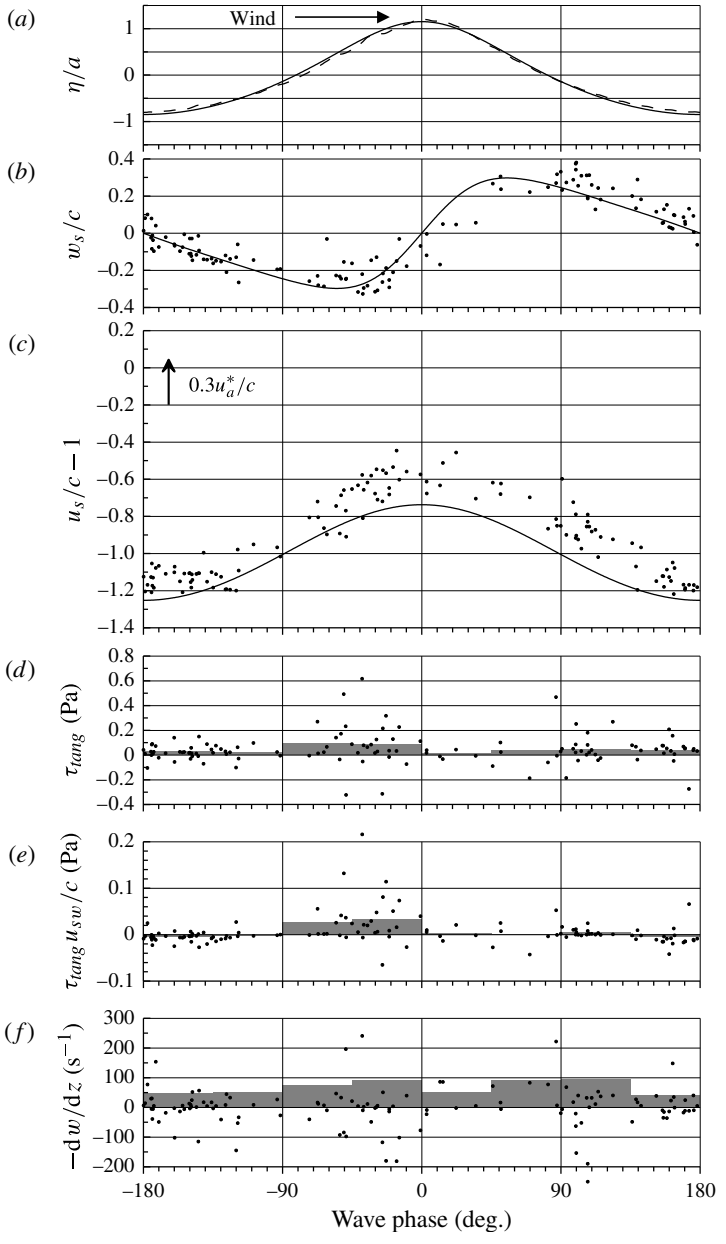

FIGURE 7. PIV surface data for experiment F31U39AK28 (microscale breaking). (*a*) A representative wave profile (dashed curve) with the corresponding fifth-order Stokes profile (solid curve). (*b*) Vertical velocity component normalized by the wave speed (points) with the fifth-order Stokes estimate (solid curve). (*c*) Horizontal velocity normalized by wave speed in a frame of reference moving with the wave (points) and fifth-order Stokes estimate (solid curve). (*d*) Surface tangential stress, instantaneous values shown as points with 45° bin averages shown as solid bars. (*e*) Wave coherent tangential stress, instantaneous values shown as points with 45° bin averages shown as solid bars. (*f*) Surface divergence, instantaneous values shown as points with 45° bin averages shown as solid bars.

the mean of all the individual data and is expressed with an uncertainty equivalent to the standard error while row 14 shows the average of the 45° tangential stress bins. The computed mean stresses are in good agreement. At the same wind speed, only small changes in the mean tangential stress are observed for different wave states despite significant changes in the visual appearance of the water surface roughness (figure 2).

As the wind stress increases, the instantaneous variability in the tangential stress also increases significantly with possible contributions from the air-side tangential stress, possible capillary wave activity or disturbances in the viscous sublayer caused by near-surface aqueous turbulent structures. Banner & Peirson (1998) observed similar scatter along the surfaces of modulating wind waves, predominantly in a microscale breaking state. It had been hoped that during this present investigation the more uniform wave fields would reduce the scatter in the measured tangential stresses. This is not observed.

In all cases, the binned tangential stress data indicate a peak at or just upwind of the wave crest. This is in agreement with the findings of Banner & Peirson (1998) for microscale breaking wind waves. Banner & Peirson (1998, § 5.2) were unable to capture many reliable tangential stress measurements on the leeward faces of the microscale waves and developed a mean profile from all experimental data coupled with flow visualization in the air. The present measurements along the leeward faces of the breaking waves suggest that the tangential stresses may be more uniformly distributed between the crest and trough (figures 4 and 6). The measurements of Veron, Saxena & Misra (2007) are in quantitative agreement with Banner & Peirson (1998) and the strong air flow separations observed may be associated with the stronger modulations in the microscale breaking wave field. Present evidence is that the spilling regions of microscale breaking waves lie within an air flow separation region in the lee of the crests and lack of sampling at these points is unlikely to introduce significant bias in the present measurements. Techniques to verify this by directly sampling the surface tangential stress within these regions remain to be developed.

Banner & Peirson (1998) explored the ratio $\tau_{\mathrm{tang}}/\tau$ as a function of a suite of non-dimensional characterizations. The mean tangential stress values were calculated for each experimental case (table 1, rows 13 and 14) with the standard errors computed as shown in table 1, row 13. Figure 7 shows the ratios of $\tau_{\mathrm{tang}}/\tau$ obtained during this present study in comparison with the data obtained by Banner & Peirson (1998) presented as a function of the wave age c/U. Figure 8 shows that for these waves which are artificially aged due to the presence of the mechanically generated waves, the stress partition is insensitive to any variation in wave age. The high steepness values ($0.24 < ak < 0.32$, table 1, row 10) place the partition data naturally amongst the other data assembled by Peirson & Garcia (2008) in their figure 5 and in strong agreement with the form drag measurements of Banner (1990).

4.1.2. *Wave-coherent tangential stress*

The skin friction contribution to wave growth has been computed for each experiment and global and binned averages are shown in row 15 and 16 of table 1. The corresponding values and binned values are shown in panel (*e*) of figures 4–7. The mean wave-coherent tangential stress in all cases reaches a maximum in the vicinity of the wave crest, as anticipated, but was less than 5 % of the total wind stress for all cases. Consequently, wave growth is dominated by the form drag.

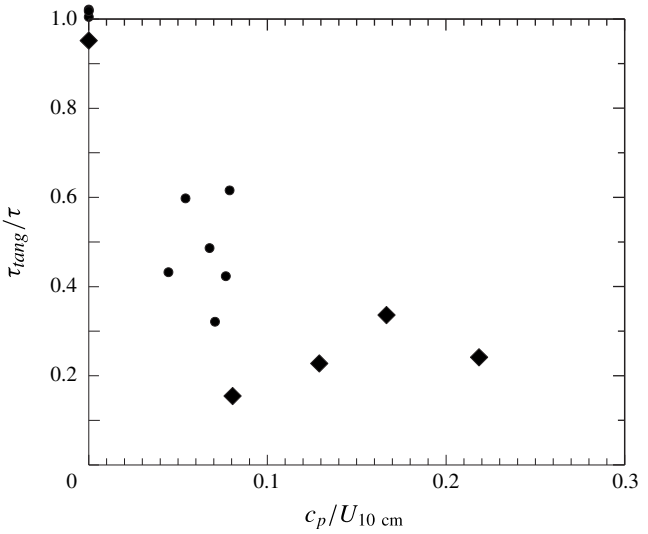

FIGURE 8. Stress partition as a function of tank wave age. Solid circles show the data of Banner & Peirson (1998) and solid diamonds show the data from the present study.

4.1.3. *Surface divergence*

Panel (*f*) of figures 4–7 shows the measured surface divergence, computed using (2.10). To set these values in the context of the larger-scale gravity wave, the magnitude of the divergence associated with a fifth-order Stokes waves of similar amplitude and wavelength is of order 3 s^{-1}. The mean values are shown in row 17 of table 1 with the standard error in the mean. In spite of the substantial number of samples obtained, these mean values are not well-determined due to the very strong fluctuations measured. The bin-averaged root-mean-square values do not show particularly systematic behaviour in panels (*f*) of figures 4–7.

The overall picture gained from these data in combination with the tangential stress data is that the localized forcing of wind-forced water surfaces is extremely vigorous: at least an order of magnitude greater than that associated with the movement of the underlying wave forms.

4.2. *Constituent exchange*

4.2.1. *Bulk measurements*

Komori *et al.* (1993) collated a range of laboratory and field data sets obtained using bulk measurement techniques. These have been used to set the context of the present data which are shown in figure 9 normalized to a Schmidt number of 600. While a limited number of wind speed cases were investigated during this study, the range of wave steepnesses employed resulted in a strong dynamic range in total stress (and therefore both air and water friction velocities). Repeat measurements of bulk gas transfer velocity showed that uncertainty in the measured bulk gas transfer velocities is less than 4 %.

These results highlight one of the fundamental difficulties in interpreting such data. Although an identical bulk wind speed was maintained within the headspace, modifying the wave forms significantly changes both the friction velocity and the

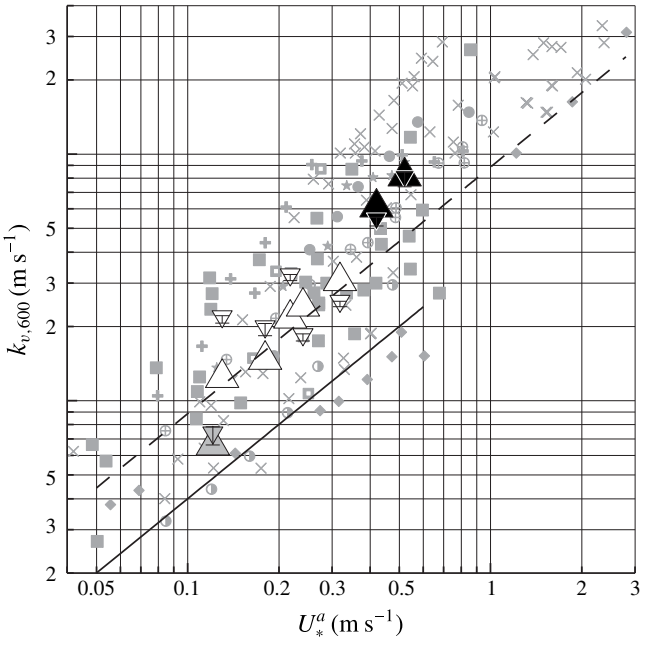

FIGURE 9. Bulk transfer velocity for the eight experimental wind-wave cases investigated in this study, normalized to a Schmidt number of 600, as a function of air friction velocity. Data in the context of the compilation by Komori *et al.* (1993) are shown as small grey symbols. Solid line shows the Deacon (1977) model (2.8). Dashed line shows the Jähne *et al.* (1987) normalization (2.12). Results from the present investigation: the large upward triangles show the bulk transfer velocity measurements and the smaller downward pointing triangles show the mean values obtained from the LIF measurements, coloured as follows: grey indicates the flat water experiments; hollow symbols show the ripple, low wave and incipient breaking cases; and the solid symbols indicate the microscale breaking data cases. Note that the ripple and non-breaking cases closely follow the Jähne *et al.* (1987) normalization. Note also the significant enhancement that occurs in the presence of microscale breaking.

transfer velocity. However, the assembly of the bulk data in figure 9 does allow some preliminary interpretations of these data to be made.

As shown in figure 9, data for the *ripple, low wave and incipient* cases are approximately co-linear, closely following the Jähne *et al.* (1987) formulation (2.12). The best fit to these specific cases yields a coefficient of 1/14.5. Consequently, little distinction can be made between these three surface conditions, prompting the conclusion that once the surface is perturbed by smaller wavelets (see figure 2), there is a common characteristic behaviour. Further, in spite of the strong well-developed parasitic capillary structures shown in figure 2(*c*,*f*), the presence of these structures does not seem to significantly enhance exchange.

Correspondingly, both the flat water and the microscale breaking cases appear to belong to two separate characteristic surface conditions, with the microscale breaking cases exhibiting a similar slope to the wavelet-perturbed conditions but with an appreciable offset in transfer velocity. The observations of a significant change in surface kinematic behaviour (Peirson & Banner 2003) and thermal behaviour (Zappa *et al.* 2004) prompts us to interpret this shift as being associated with microscale

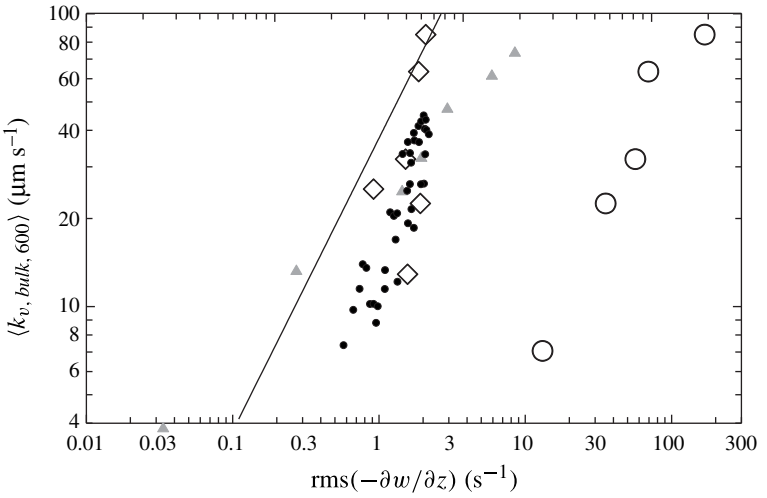

FIGURE 10. Bulk transfer velocity normalized to a Schmidt number of 600 as a function of surface divergence. Solid circles show the cluster of data from McKenna & McGillis (2004), their figure 9, and grey triangles show the measurements of Turney *et al.* (2005), their figures 2b and 3b. Diamonds and hollow circles indicate data from this study by the approximate gravity wave r.m.s. divergence or the localized PIV divergence respectively. Solid line is the Ledwell (1984) formulation.

breaking. As discussed earlier, our recent work shows that a significant shift in Schmidt number occurs from the flat water to the capillary ripple condition (Yan *et al.* 2011), supporting our conclusion that the flat water condition should be regarded differently from the remainder of the data.

McKenna & McGillis (2004) have proposed an alternative parameterization based on surface divergence, (2.15). Our data are presented with the cluster of their data in figure 10, which has been recomputed to a Schmidt number of 600 using (2.13) with $n = 0.5$. Also shown is a compilation of data obtained from Turney *et al.* (2005).

Computations of the root-mean-square divergence due to the underlying irrotational gravity waves using a fifth-order Stokes description of the surface velocity shows differences of only about 10 % from the simple expression:

$$rms\left(-\frac{\partial w}{\partial z}_{wave}\right) = 4akf. \tag{4.1}$$

The present data are also shown in figure 10 using this approximate expression for the surface divergence. They sit in reasonable proximity to the McKenna & McGillis (2004) and Turney *et al.* (2005) data, except for the continuously microscale breaking cases of the present experiments which indicated a significant relative enhancement in comparison with the other measurements. Note that the flat water case cannot appear in this normalization although it has a characteristic $k_{v,600} = 7.1$ μm s^{-1} in this normalization.

McKenna & McGillis (2004) show that the formulation of Csanady (1990), which was developed for microscale breaking conditions, is of the same form as Ledwell (1984), Banerjee *et al.* (2004) and Turney *et al.* (2005) but with an additional enhancement factor of $\sqrt{\pi/2} = 1.25$. Incorporating this relative enhancement of the

exchange factor would provide a plausible reconciliation between the microscale breaking data and the other data obtained during this study.

The alternative means of presenting the data is to use the directly measured divergence available from the PIV data. As shown in figure 10, the r.m.s. magnitude of this localized divergence exceeds the gravity wave component by approximately one order of magnitude. While the collapse of the present data (including the flat water and microscale breaking cases) looks promising, this approach does not reconcile these measurements with those of McKenna & McGillis (2004) and Turney *et al.* (2005). Using order-of-magnitude analysis, Peirson & Banner (2003) found that surface divergence was not anticipated to play a major role in determining surface flux for microscale breaking conditions, and the dominant processes were advection relative to the wave forms and molecular diffusion. Reconciliation of these issues may require consideration of the relevant length scales: the gravity waves in this study have a length scale of order 0.1m and PIV resolution is order 0.05 mm while the surface motions observed by McKenna & McGillis (2004) had length scales of 0.01 m and PIV resolution of 1 mm (their figure 7). Figure 1 in Turney *et al.* (2005) indicates length scales of order 0.07 m with a PIV resolution of 1 mm.

As discussed in the introduction, the toes of breaking waves may be considered as convergence lines traversing the surface. Therefore, quantifying surface convergence for surfaces that feature microscale breaking waves may be sensitive to the characteristic length scale of the measurements.

4.2.2. *LIF measurements*

With the exception of the capillary ripple experiments, our present experimental configuration allowed us to determine the phase of the near-instantaneous LIF measurement along any underlying gravity wave. The triggering system permitted capture of images in close proximity to the crest, trough and mean water level on the windward and leeward wave faces.

For each wind and wave condition, approximately 400 images (table 2, row 4) were captured and analysed to determine constituent transfer at the air–water interface after the careful checking procedures described in Walker & Peirson (2008). As with the PIV image processing, under conditions of stronger forcing, the surface was more ruffled and this decreased the relative proportion of captured images in which clearly visible reflections of the ADS could be identified. The statistics in row 4 of table 2 show the impact of this effect for each of the experimental cases, and a reduced number of processed images is particularly noticeable in Experiment F34U57AK32. Consequently, we conclude that a wind speed of approximately 5.5 m s^{-1} (U_{10} = 13.4 m s^{-1}) is the maximum level of surface forcing in which the present technique can be applied reliably. As shown by Walker & Peirson (2008), the key aspect needed to apply these techniques to higher wind forcing conditions is further improvement in the optics to decrease the waist of the light sheet in the vicinity of the interface.

The mean flux measurements obtained from LIF match the bulk measurements within 30 % with the exception of Experiments F34U21AK18 and F34U21AK27. For these two experiments, the LIF method overestimates the flux by 65 % and 41 % respectively (table 2, rows 3, 5 and 7; figure 9). There are three potential contributions to the differences between the LIF and bulk results for all experiments:

(i) Unquantified optical diffraction within the lens system. The impact of optical diffraction would be to reduce systematically curvatures in the measured vertical concentration profiles in the vicinity of the interface. This effect would be anticipated to result in systematic underestimates in the measured LIF flux, (2.4).

https://doi.org/10.1017/jfm.2013.681 Published online by Cambridge University Press

	Experiment	F00U21AK0	F34U21AK18	F34U21AK27	F34U57AK32	F63U42AK00	F21U39AK10	F24U39AK24	F31U39AK28
1	Surface	flat water	low	incipient	microscale	ripple	low	incipient	microscale
2	Temp. (°C)	19.3	19.1	19.1	18.4	18.4	18.3	17.3	17.0
3	k_{vbulk} (m s^{-1} $\times$ 10^6)	7.57	13.8	24.0	88.6	16.0	26.2	32.2	63.4
4	LIF images accepted	71				163			
	crest		111	78	7		121	94	115
	leeward		120	159	22		183	135	91
	trough		135	105	27		153	190	148
	windward		125	129	27		189	170	97
5	LIF k_{vlif} (μm s^{-1})	7.94 ± 0.6	22.8 ± 1.4	33.7 ± 1.8	82.5 ± 11.0	20.3 ± 1.1	18.8 ± 1.2	24.9 ± 1.3	53.2 ± 4.4
	crest		23.8 ± 1.3	21.2 ± 1.6	45.6 ± 10.4		17.0 ± 1.1	19.5 ± 1.0	39.4 ± 3.5
	leeward		24.9 ± 1.8	34.9 ± 1.7	84.7 ± 12.8		19.7 ± 1.0	28.4 ± 1.4	47.0 ± 4.0
	trough		23.6 ± 1.6	58.0 ± 3.0	138 ± 15.1		20.1 ± 1.8	28.1 ± 1.2	70.3 ± 4.1
	windward		18.7 ± 1.1	20.6 ± 1.0	61.5 ± 5.6		18.5 ± 1.1	23.4 ± 1.4	56.0 ± 5.8
6	σ $(ln(k_{\mathrm{vlif}}))$	0.579	0.654	0.667	0.668	0.489	0.591	0.514	0.763
7	k_v % diff LIF–bulk	5	65	41	−7	27	−28	−23	−16
8	$z^+_{95\,\%}$	2.3				4.3			
	crest		1.5	3.5	9.8		4.2	4.1	6.8
	leeward		4.1	2.9	2.7		3.2	3.6	2.8
	trough		4.2	4.3	5.7		8.9	7.5	8.3
	windward		4.0	7.1	8.3		4.6	7.3	10.4
9	$\hat{C}_{100\ \mu\mathrm{m}}$	0.32				0.48			
	crest		0.50	0.46	0.74		0.52	0.60	0.69
	leeward		0.48	0.55	0.77		0.60	0.62	0.85
	trough		0.45	0.78	0.88		0.57	0.63	0.86
	windward		0.42	0.40	0.76		0.55	0.57	0.78

TABLE 2. Summary of flux measurements.

(ii) The bulk aeration transfer velocity is derived from contributions from the entire tank surface area. In spite of our objective to minimize variations in wind and wave conditions along the tank, there is some minor fetch development of wave group structures. The surface area of the emergent laser sheet is a tiny (3×10^{-7}) proportion of the total surface area over which gas exchange occurs in the wind-wave tank.

(iii) The standard deviations of the measured instantaneous transfer velocities are greater than 50 % of the mean values for all measurement cases, implying significant variability in the fluctuating transfer velocities. However, the standard errors shown in row 5 of table 2 indicate that inadequate sampling does not appear to be the source of these discrepancies.

Nonetheless, these measurement developments improve substantially the accuracy of the technique of Woodrow & Duke (2001) who reported differences of up to 140 % between LIF and bulk measurements obtained in much shallower depths of water and much closer proximity to the tank wall.

The mean of the LIF transfer velocities did not drift significantly in time during each of the experiments (for details see Walker 2009). This demonstrates that the measurement technique was not sensitive to the changing dissolved oxygen concentrations in the water nor was there any significant shift in the surface conditions during the experiments.

Figure 11 shows an assembly of the probability distributions for the each of consolidated data sets. These show that the transfer velocity probability distributions conform to log-normal form. A remarkable feature of this assembly is that the standard deviation of the quantity $\log_e(k_v)$ maintains a consistent value of $0.62 \pm 0.15(\log_e(\mathrm{m\ s^{-1}}))$ and does not show any strong systematic change that can be correlated with the surface forcing. Further, these distributions show no systematic decline in the transfer velocity within the tails of the distribution, showing that the extreme values have been adequately captured by these measurement techniques. The tails of the microscale breaking cases contain instantaneous transfer velocity measurements in excess of 0.2 mm $\mathrm{s^{-1}}$, comparable with the highest bulk values shown in figure 9 when adjusted for the change in Schmidt number.

Given the conclusion of Peirson & Banner (2003) that microscale breaking waves should have a distinctly different signature from those of non-breaking waves, these results were initially disappointing. However, as discussed below, present evidence is that the microscale breaking is not as efficient as first thought and its signature is masked by other competing wave-related processes.

Woodrow & Duke (2001) and Takehara & Etoh (2002) observed detached surface layers of constituent-rich water. These also were observed in approximately 25 % of all images captured during this investigation. However, no significant correlation was observed during this present study between the occurrence of detached surface layers and the high constituent gradients at the surface.

Two other statistics have been used to characterize the overall size of the ADS. The 95 percentile bulk dissolved oxygen concentration was directly measured from the concentration profile of each LIF image and the depth recorded. The 95 percentile dissolved oxygen concentration is defined as:

$$\hat{C}(z) = \frac{C_I - C(z)}{C_I - C_B} \tag{4.2}$$

and $z^+_{95\%} = z_{95\%} u^w_* / \nu$ is the normalized distance below the surface at which $\hat{C}(z) = 0.95$ in (4.2). The mean $z^+_{95\%}$ value for each experiment is tabulated in table 2, row 8.

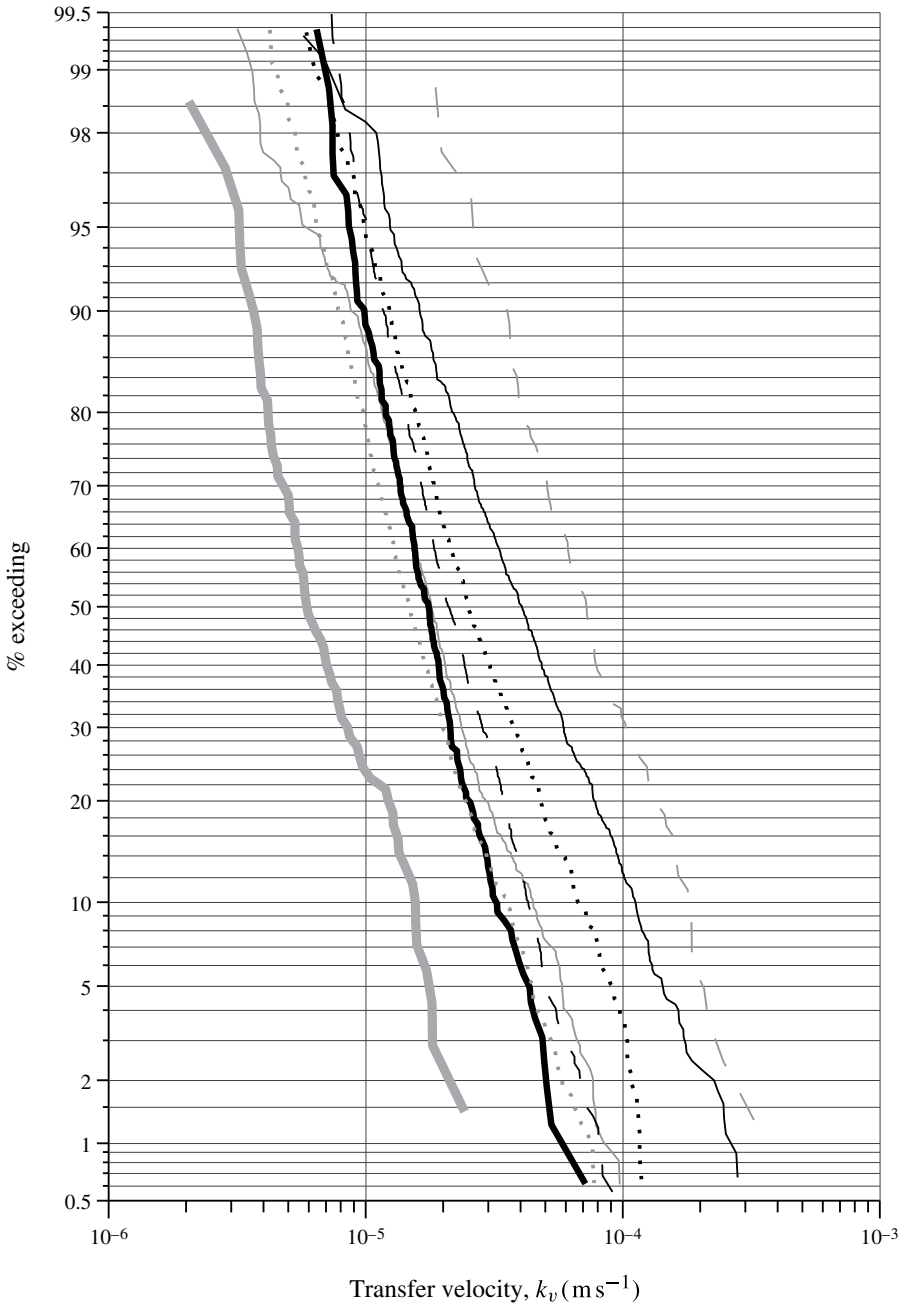

FIGURE 11. Cumulative probability distributions of instantaneous k_v measurements for all cases. Reading along the median transfer line, the cases are as follows: grey heavy solid line, F00U21AK0 (flat water); grey dotted line, F21U39AK10 (low wave); black heavy solid line, F63U42AK00 (capillary ripples); grey light solid line, F34U21AK18 (low wave); black dashed line, F24U39AK24 (incipient breaking); black dotted line, F34U21AK27 (incipient breaking); black light solid line, F31U39AK28 (microscale breaking); grey dashed line, F34U57AK32 (microscale breaking).

Almost the entire ADS is nestled within the aqueous linear sublayer (Banner & Peirson 1998, p. 131). The data show that, in general, the ADS is shallowest on the leeward face of the waves and the crest thickness is thinner than the trough thickness, providing further evidence that the overall thickness of the ADS is controlled by processes local to the wave crests.

While the measured depth at which the 95 percentile dissolved oxygen concentration occurs contributes to the understanding of hydrodynamic behaviour beneath waves, it cannot be used as a reliable indicator of the gas transfer velocity across the interface. Any dimensionless dissolved oxygen concentration measurement that is used for this purpose would need to be undertaken immediately adjacent to the surface where molecular rather than turbulent diffusion is the dominant process.

Given the profound difficulty of capturing reliable concentration profiles adjacent to a free surface and that a dissolved oxygen concentration gradient was still evident at a depth of 100 μm, each LIF image was analysed to determine the dimensionless dissolved oxygen concentration at $z = 100\ \mu\text{m}$ $\left(\hat{C}_{100\mu m}\right)$. Some investigators have developed simpler techniques capable of capturing concentrations at this depth (Jirka & Ho 1990). A best-fit expression was developed for the measured mean dimensionless dissolved oxygen concentration values, $\hat{C}_{100\mu m}$, as a function of the calculated mean gas transfer velocity derived by LIF (k_{vlif}) for each experiment and this yielded:

$$k_v = 3.44 \times 10^{-6} \times \mathrm{e}^{\left(3.59\hat{C}_{100\mu m}\right)}. \tag{4.3}$$

The clearest (and unanticipated) signature in the LIF data was the strength of modulation of the transfer velocities along the wave forms. From earlier work, it had been anticipated that the highest transfer velocities would be found at the wave crests of the microscale breaking waves but this was not the case as illustrated in figures 12 and 13. Mean transfer velocities were systematically higher in the troughs than those observed at the wave crests and this difference increased with wave steepness (table 2, row 5 and figures 12 and 13). Transfer velocities measured on the leeward and windward limbs of the waves are almost always bounded by the upper and lower values obtained at the wave troughs and crests. Thinner diffusion sublayers in the wave troughs were visually apparent in the LIF images prior to any processing.

These results formed the basis of a quantitative decomposition of the constituent flux as described as follows.

4.3. *Quantitative decomposition of the constituent flux*

4.3.1. *Orbital straining of near-surface fluid elements by waves*

The strongest phase-related signature in the LIF data is the modulation that occurs along the gravity wave forms which intensifies as the waves steepen (e.g. figure 13). To quantify the significance of this process for each experiment in which gravity waves were present, the phase-related data shown in row 5 of table 2 have been normalized by the global mean value of k_v and plotted as a function of ak in figure 14. In each case, the standard error is shown to indicate the level of uncertainty in each data point.

As anticipated, values obtained in the vicinity of the leeward and windward mean water level positions remain in reasonable proximity to the global average value in each case with no systematic change with wave steepness apparent. Systematic development of crest and trough transfer velocities can be observed in figure 14

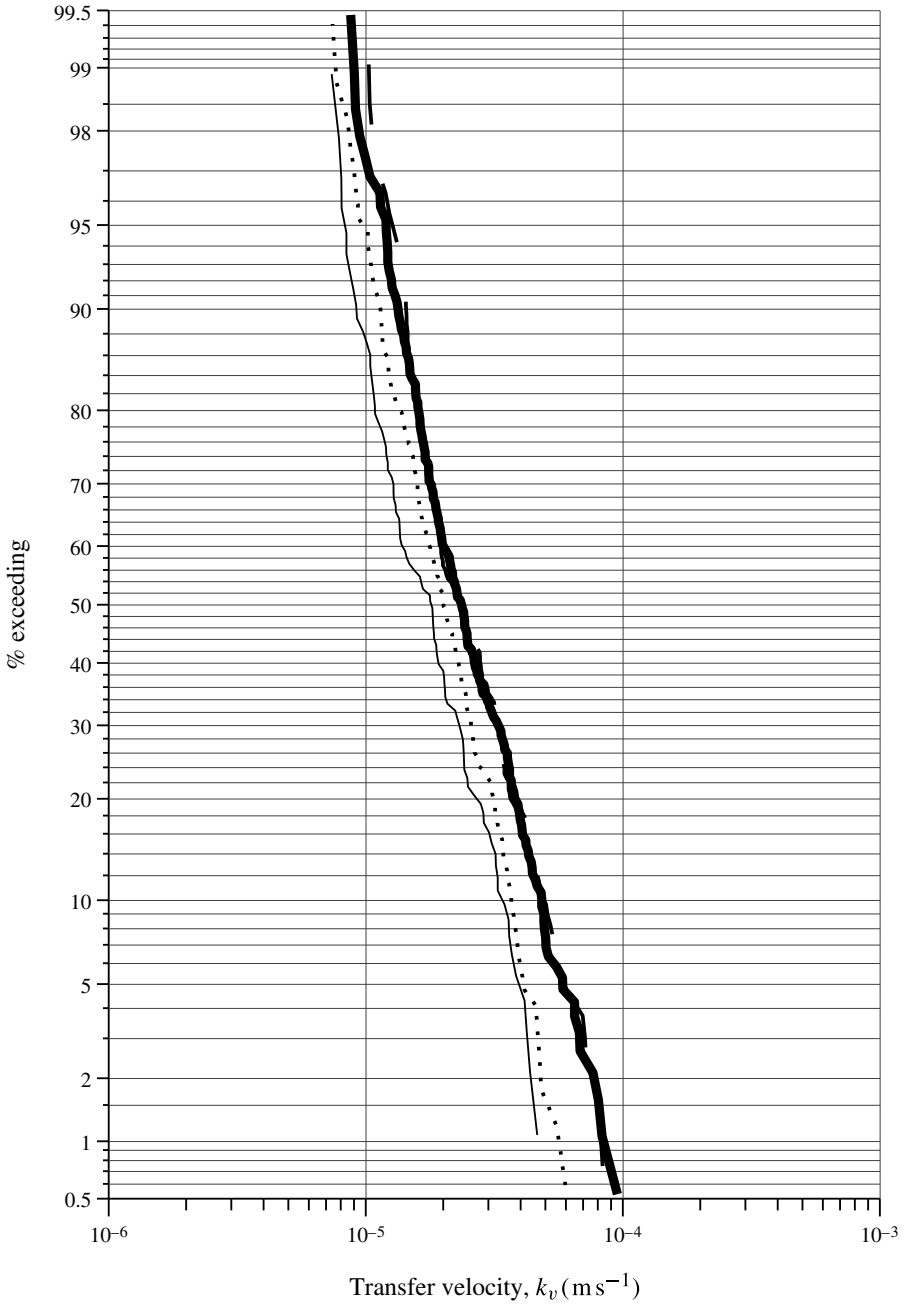

FIGURE 12. Cumulative probability distributions for instantaneous k_v measured during experiment F24U39AK24 (incipient breaking): heavy solid line, wave trough; light solid line, wave crest; dotted line, windward face; dashed line, leeward face.

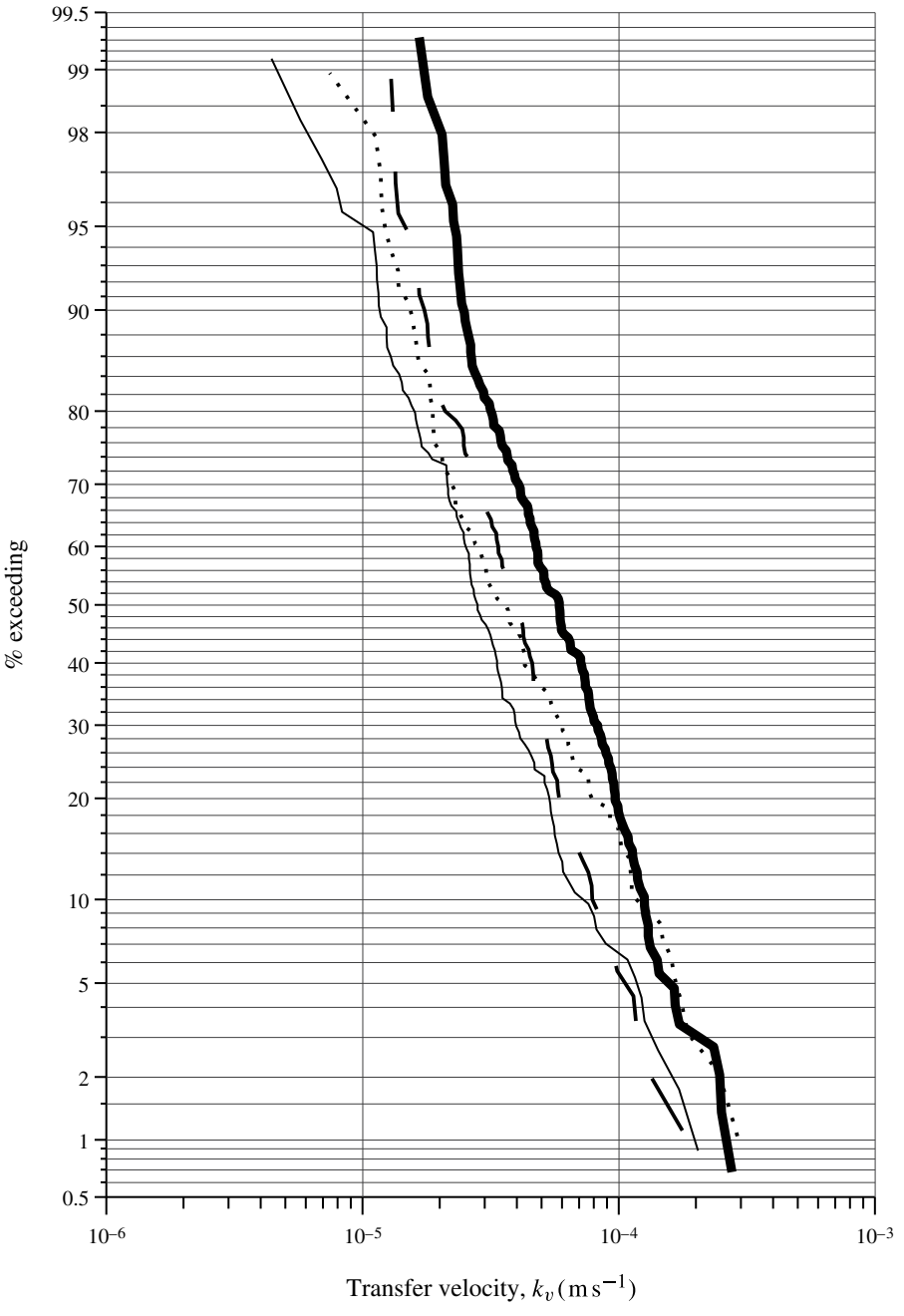

FIGURE 13. Cumulative probability distributions for instantaneous k_v measured during experiment F31U39AK28 (microscale breaking): heavy solid line, wave trough; light solid line, wave crest; dotted line, windward face; dashed line, leeward face.

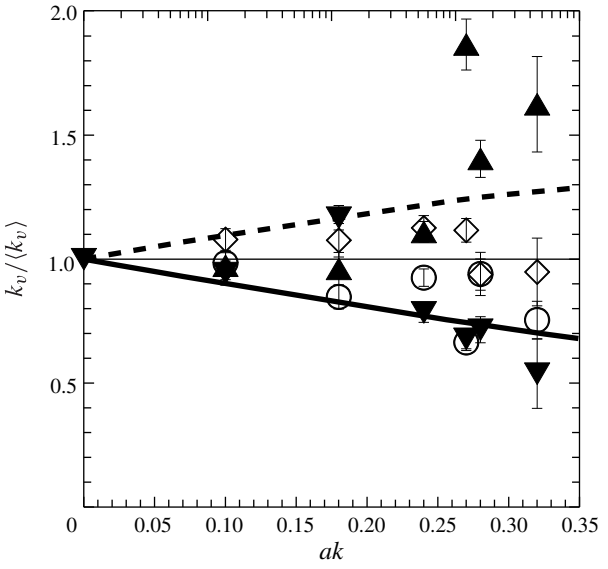

FIGURE 14. Local phase-related transfer velocity as a function of underlying gravity wave steepness normalized by the global mean of all measurements for each experimental case. Solid upward triangles, wave troughs; solid downward triangles, wave crests; hollow diamonds, windward face at the mean water line; hollow circles, leeward face at the mean water line. Solid and dashed lines indicate predictions using the theory of Witting (1971) and fifth-order Stokes theory for the troughs and crests respectively.

with increasing steepness, as anticipated by Witting (1971). Witting assumed that the constituent gradient at and normal to the local surface was subject to orbital straining and in accordance with stagnant film theory (equation (2.4) (see also Witting 1971, equation (2.18)).

In figure 14, the predicted normalized crest and trough transfer velocities are presented as a function of mean wave steepness. These were obtained using the same approach as Witting but using the fifth-order Stokes theory of Skjelbreia & Hendrickson (1961). It can be observed that, in spite of the theoretical simplicity of this approach, it does provide a reasonable representation of the observed phase-related behaviour.

The observed agreement between the measurements of a systematic phase-related behaviour based on irrotational wave and stagnant film theories points to localized rather than diffuse control of the surface concentration gradient. The work of Longuet-Higgins (1992) and Peirson & Banner (2003) and the present investigation all show that peak near-surface shears due to mediation of wind-induced shear stresses occur in proximity to the crests of the waves. Gemmrich (2010) has recently found similar behaviour beneath large-scale waves in the field.

In contrast with the surface concentration gradient, the overall thickness of the ADS (as quantified by $z^{+}_{95\,\%}$, table 2, row 8) shows phase-related behaviour that is incompatible with an irrotational behaviour. The ADS thickness tends to be thinner at the crests than the troughs, pointing to enhanced mixing in proximity to the crests. This observation is entirely compatible with the conclusions of the physical investigations described in the previous paragraph.

In Witting's analysis, the mean surface concentration gradient in the presence of wave forms is referenced to the mean water level (Witting 1971, p. 325, first paragraph). Such an approach may not be applicable for wind-forced waves where the evidence suggests that the surface concentration gradients are determined by processes local to the wave crests and any imposed orbital wave straining systematically increases the total constituent flux. Constituent flux enhancement for wind waves by gravity orbital straining is therefore higher than previously anticipated by Witting (1971), Deacon (1981), Csanady (1990) and Jähne & Haußecker (1998), amongst others.

Two effects are operative: the presence of the waves increases the surface area of the waves and the orbital straining of the waves leads to a net increase in the mean surface concentration gradient. Taking a similar approach to Witting, the total transfer velocity k_{v_total} is therefore computed as a function of a transfer velocity that excludes orbital straining ($k_{v\_non\_orbital}$) enhanced by a contribution due to wave orbital-related processes W:

$$k_{v\_total} = W k_{v\_non\_orbital}. \tag{4.4}$$

Using fifth-order theory as an approximation and numerically integrating the local enhancement due to orbital straining and surface dilation along the wave (Witting 1971, equation 2.19) yields:

$$W = 1.00 + 0.97ak + 1.41\,(ak)^2\,. \tag{4.5}$$

The linear term in (4.5) does not appear in Witting (1971, equation 5.3), and emerges because here the wave enhancement is referenced relative to conditions at the wave crest rather than at the mean water level as assumed by Witting. As noted by previous investigators, dilation of the wave surface is a minor effect, contributing approximately 10 % of the total enhancement. For a notional maximum wave steepness of $ak = 0.446$ the effective enhancement is now 1.71, almost a factor of 2 higher than the enhancement predicted by Witting (1971).

It is interesting to note that recent work of Veron, Melville & Lenain (2008) has investigated wave-related enhancement of heat fluxes under field conditions. They find that the wave-related contribution increases with the mean-squared slope of the wave field rather than linearly with wave slope as shown in (4.5). Also, the enhancement as a function of wave slope is much more modest than is found here.

The LIF gas transfer velocity data and the 95 percentile dissolved oxygen concentration data highlight the complexities of the hydrodynamic behaviour beneath wind-driven waves. From the PIV experiments it was shown that the highest tangential stresses were measured near the crests of the waves and the lowest tangential stresses were measured in the wave troughs. The combined perspective gained from the LIF and PIV data indicates that, at depth, the turbulence has a significant role in mixing of the water column. However, very close to the surface, where viscosity dominates, the influence of wave orbital straining would appear to have a more pronounced influence on the gas transfer velocity than the underlying turbulence. Hence, the 95 percentile dissolved oxygen concentration is generally shown to be closer to the surface at the wave crests than the wave troughs (presumably due to turbulence), but the mean gas transfer velocity in the wave troughs is greater than the mean gas transfer velocity at the wave crests (due to wave orbital straining of the aqueous diffusion sublayer). There are contrasting behaviours within the ADS between immediate proximity to the interface and the outer limits of the sublayer itself. Few studies have quantitatively examined turbulent mixing beneath breaking wind waves and further investigation would shed light on these specific issues.

4.3.2. *Turbulent and capillary ripple contributions*

For Experiment F00U21AK0 (*flat water*) the transfer velocity measured by both the bulk and LIF methods is approximately 1.4 times that predicted by Deacon (1977). Although questionable due to its basis on boundary layer theory at a solid wall and neglect of surface convergence and divergence, Deacon's model has remained a reference point for subsequent studies up to the present (e.g. Wanninkhof *et al.* 2009).

The present data demonstrate that fluctuations in surface velocity (table 1, row 12) for the *flat water* case occur with a standard deviation of approximately 17 % of the mean. This may explain the differences observed between Deacon's model estimate and the mean observed transfer velocity as measured by both the bulk and LIF methods. The techniques developed during this study may also provide a route to quantifying systematically the influence on flux rates through contamination by arresting surface motions.

Careful inspection of the images shown in figure 2 reveals that the freely propagating capillary ripples and parasitic capillary waves developed naturally for all test cases except for the flat water condition.

Ignoring the microscale breaking cases (which are presumably impacted by the breaking process) and the flat water condition, the bulk transfer velocities obtained from the remainder of the test cases showed good collapse in figure 9 as a function of friction velocity. While the microscale breaking data show a distinct shift from the trend of the non-breaking data in figure 9, no similar distinct shift can be observed associated with the development of strong parasitic capillary structures (figure 2).

Therefore quantifying localized enhancement of transfer velocity specifically related to parasitic capillary development (if it does occur) will require much more precise measurement techniques than were available during this study. In this present decomposition, we have no alternative but to incorporate any enhancement of near-surface mixing due to these small-scale waves into that due to subsurface turbulence (see also Csanady 1990, p. 576 comments on *wavulence*).

The transfer velocity without wave orbital straining enhancement $k_{v\_non\_breaking}$ is therefore partitioned into two components: a contribution due to subsurface turbulence and the wavelets, $k_{v\_turb,ripple}$, and a component due to breaking, $k_{v\_breaking}$, that is:

$$k_{v\_total} = Wk_{v\_non\_orbital} = W\left(k_{v\_turb,ripple} + k_{v\_breaking}\right). \tag{4.6}$$

The orbital contribution was determined using (4.5) (table 3, column B) was removed for the non-microscale breaking cases and then an equation of similar form to (2.12) is fitted to the balance by least squares yielding:

$$k_{v\_turb,ripple} = \frac{1}{17.3} Sc^{-1/2} u_*^w. \tag{4.7}$$

This reduces the coefficient in (2.12) slightly from 1/14.5 to 1/17.3. The transfer velocity contribution between the orbital-related $((W-1)k_{v\_total}/W)$ and turbulent/capillary-wave-related (4.7) components is shown in columns B and C of table 3. As shown in table 3 (columns G and H), the wave orbital component is a non-negligible contribution to the total flux. The 'misclose' (the difference between the total flux and sum of the partitioned components) demonstrates the good degree of fit to the data with the determined coefficient of 1/17.3 and this normalization.

https://doi.org/10.1017/jfm.2013.681 Published online by Cambridge University Press

		$k_{v,600}$ (μm s^{-1})					Partition				
		A	B	C	D	E	F	G	H	I	J
Condition	Experiment	Total	Wave orbital	Turbulent/ripple	Breaking	Misclose	Total	Wave orbital	Turbulent/ripple	Breaking	Misclose
Flat water	F00U21AK0	6.9	0.0	9.9	0.0	−3.0	100 %	0 %	144 %	0 %	−44 %
Low wave	F34U21AK18	12.9	2.3	10.7	0.0	0.0	100 %	18 %	82 %	0 %	0 %
Incipient	F34U21AK27	22.5	6.0	17.9	0.0	−1.3	100 %	26 %	79 %	0 %	−6 %
Microscale	F34U57AK32	84.9	26.4	42.6	14.0	1.9	100 %	31 %	50 %	17 %	2 %
Ripple	F63U42AK00	15.3	0.0	14.8	0.0	0.6	100 %	0 %	96 %	0 %	4 %
Low wave	F21U39AK10	25.2	2.5	19.7	0.0	3.0	100 %	10 %	78 %	0 %	12 %
Incipient	F24U39AK24	31.9	7.6	26.1	0.0	−1.7	100 %	24 %	82 %	0 %	−5 %
Microscale	f31U39AK28	63.5	17.5	34.4	13.4	−1.8	100 %	28 %	54 %	21 %	−3 %

TABLE 3. Gas transfer velocity as measured at the wave crests and wave troughs by the LIF method and the theoretical enhancement due to orbital straining.

4.3.3. *Microscale breaking contribution*

Having determined appropriate levels of wave orbital and turbulent/capillary ripple contributions to the total flux, these values can be extrapolated appropriately to determine these contributions in the presence of microscale breaking conditions.

Peirson & Banner (2003) predicted subduction of the aqueous diffusion sublayer at the onset of microscale breaking from their observations of near-surface velocity structure. If all waves were in a continuous microscale breaking state, we would expect to only see very thin diffusion sublayers. Consequently, distinct population boundaries would be evident between the incipient and microscale breaking cases but this is not supported by the distributions shown in figure 11. If microscale breaking waves are constantly collapsing and re-forming into a breaking state, the microscale breaking cases may consist of two data populations: very thin diffusion sublayer thicknesses associated with recent subduction events and more developed profiles transiting the breaking regions during periods of relaxation of the breaking. This is a better characterization of the distributions presented in figure 11.

By extracting orbital straining ((4.4), table 3, column B) and the turbulent/ripple ((4.6), column C) contributions from the total constituent flux rates of the microscale breaking data and comparing with (2.18), an efficiency of $e = 17 \pm 2\,\%$ is obtained. Using the mean value of efficiency to estimate the microscale breaking contribution in (2.18), the budget partitions, with their corresponding miscloses, are finalized in table 3.

While the turbulent/ripple contribution remains dominant for the microscale breaking conditions, its total contribution has now fallen to 50 %, with the wave-related components accounting for the other half of the total flux.

Although these microscale breaking efficiency rates are more modest than anticipated in Peirson & Banner (2003), the present data provide new key insights for constituent exchange models.

Phillips (1985, p. 527) defined a mean turnover rate per unit time, $c\Lambda(c)\mathrm{d}c$, which is the spectral equivalent of f in (2.17). Hence we can quantify the additional enhancement due to breaking as:

$$k_{v,breaking} = (1.075 \pm 0.075)\sqrt{D \int ce^2\,(c)\ \Lambda\,(c)\ \mathrm{d}c}. \tag{4.8}$$

Motivated by Phillips (1985), field measurements of the distribution $\Lambda(c)$ have attracted considerable recent research effort (e.g. Melville & Matusov 2002; Gemmrich, Banner & Garrett 2008; Kleiss & Melville 2010). This approach has the potential for remotely estimating wave breaking energy and momentum budgets, for which $\Lambda(c)$ is weighted by c^5 and c^4 respectively. These strong weightings of the wave speed c emphasize the contributions of the larger breaking wave scales. In (4.8), the linear-c weighting for the gas transfer rate indicates a potentially greater role for the shorter scales for this process. However, measuring $\Lambda(c)$ at short scales using visible imagery is more difficult because short-scale waves entrain considerably less air. This will be addressed through future infrared imagery field observations (e.g. Jessup 1996). Also, we note that in (4.8) we have elected to express the efficiency as a function of wave speed, anticipating that the efficiency of breaking with air entrainment may differ from that of microscale breaking.

Estimating breaking efficiencies based on visual observation of microscale breaking remains an unsatisfactory approach as actual subduction of the surface is not directly measured. The application of infrared tracer techniques and imagery to the air–water

interfaces should be able to quantify directly subduction and consequent microscale breaking efficiency factors. The lack of this quantitative information is a significant gap in the present study.

4.4. *Scatter in constituent exchange data*

In the previous section, a decomposition of constituent flux data was presented in terms of orbital, turbulent/ripple and microscale breaking contributions. In terms of figure 9, significant scatter can be observed across the assembled data. What are the primary causes of this scatter beyond inherent experimental uncertainty?

First, the encouraging consistencies of the findings of the Heidelberg group (Professor Jähne and his co-workers) with the present findings must be observed. These results are in very close agreement with their observations in two important ways:

(i) Our recent work shows an almost identical transition in Schmidt number at low levels of wind forcing (Jähne & Haußecker 1998, figure 2; Yan *et al.* 2011).

(ii) The normalization of our non-microscale breaking data (4.3) is in agreement with the Jähne *et al.* (1987) normalization (2.17) within 3 %.

Such agreement is remarkable given the significant geometric differences between the facilities used for these investigations. The use of annular flumes and tanks can induce unwarranted secondary circulations in laboratory studies and agreement between results from this linear facility and the Heidelberg annular facility is reassuring.

If issues are excluded that are associated with the Schmidt number transition at low wind forcing and surface contamination effects, the findings of this investigation that both larger-scale wave energy density and transitions to microscale breaking may provide part of the explanation to the observed scatter. This will be important both in the laboratory and the field. At larger wave scales, the breaking of smaller wave scales is promoted by the underlying swell (see Banner & Peirson 1998, figure 1 and the photo on the front cover of Thorpe 2005). Consequently, it is anticipated that for the larger wave scales, the ADS thickness will continue to be controlled by crest-related processes. Further, the time scales of constituent diffusion (approximately 48 s for 0.5 mm of molecular diffusion of CO_2 in seawater) are significantly greater than those associated with ocean swell, therefore all waves within an open ocean spectrum would be anticipated to provide some orbital enhancement. We note that the Jähne *et al.* (1987) expression ((4.5) herein, and with our modified coefficient of 1/17.3), represents exchange in the absence of orbital and microscale breaking processes and provides a natural lower bound to the data shown in figure 9 above a value of $u_*^a = 0.5$ m s^{-1}.

The present results and the findings of Banner & Peirson (1998) point to significant fetch dependence in laboratory tanks as observed by Wanninkhof & Bliven (1991). As shown in figure 9(*b*) of Banner & Peirson (1998), short tanks with naturally forming wind waves exhibit rapid development of the total wind stress with fetch. Further, the fetch dependence of wind-wave systems implies spatial gradients in orbital- and microscale-breaking-related constituent flux enhancements as well as imbalances in the air- and water-side friction velocities (2.9). Investigators may significantly bias their friction velocity values and transfer velocities if such effects are ignored.

In this present study, the microscale breaking condition has been carefully partitioned and has been shown to significantly enhance the transfer velocity. Studies that neglect this process at stronger levels of wind forcing will be vulnerable to scatter that cannot be resolved using conventional techniques.

5. Conclusions and recommendations

A detailed investigation of the mechanical and low-solubility gas coupling between wind and water has been completed in the laboratory using a suite of microphysical measurement techniques. Under a variety of wind conditions and in the presence and absence of mechanically generated short waves, approximately fetch-independent surface conditions were obtained in the laboratory over total fetch lengths of several metres.

This investigation supports the conclusions of Banner (1990) and Banner & Peirson (1998) and extends their findings to the coupling of wind with small-scale monochromatic wind waves. Specifically, the tangential stress is shown to decrease from equivalence with the total stress in the absence of waves to approximately 20 % of the total stress in the presence of small waves of mean steepness $O(0.27)$. The wave-coherent tangential stress is again found to be small at these high steepnesses.

The surface kinematical behaviour of these small waves is consistent with the observations of Peirson & Banner (2003). The measured wind-induced surface drift varied from $(0.20 \pm 0.06)u_*^a$ in the wave troughs increasing to $(0.33 \pm 0.07)u_*^a$ at the wave crests, slightly extending the variability in the troughs in comparison with Peirson & Banner (2003). Using mechanically generated waves has not eliminated the phase-related scatter observed by Banner & Peirson (1998) and improved techniques for enlarging the measurement ensembles should be developed. Nonetheless, the mean values of surface velocity drift and tangential stress are consistent with these earlier studies.

The bulk observations of re-aeration of this present investigation are consistent with previous laboratory studies. Notably, the consistency between the present linear tank measurements and previous fetch-independent measurements in annular tanks reassures investigators that there do not appear to be specific experimental artefacts induced by tank geometry.

McKenna & McGillis (2004) and Turney *et al.* (2005) proposed that surface convergence plays a primary role in constituent exchange. This proposal is critically reviewed using the microphysical surface convergence measurements obtained during this present study. Normalizations using surface convergence computed from the larger-scale wave forms do compare favourably with their results and the enhancement observed at the onset of microscale breaking does compare favourably with the enhancement which would be obtained by differencing the theoretical predictions of Csanady (1990) and Ledwell (1984). However, the microphysical measurements of localized surface convergence do not reconcile the present flux measurements with those of McKenna & McGillis (2004) and Turney *et al.* (2005) and may indicate sensitivity to spatial resolution of the surface divergence measurement.

Across the range of laboratory wind and wave conditions investigated in this study, local constituent transfer rates quantified by laser-induced fluorescence techniques show that instantaneous measurements of transfer velocity remain approximately log-normally distributed with an approximately constant standard deviation of $0.62 \pm 0.15(\log_e(\mathrm{m\ s^{-1}}))$. The mean values of transfer velocity obtained using the laser-induced fluorescence technique were reconciled with the corresponding bulk measurements of constituent transfer and showed significantly improved accuracy in comparison with previous studies. However, some significant disparities remained between the localized and bulk measurements of mean transfer and there are specific limitations in the technique developed in the present study. Further studies with increased ensemble size and improved refinements to the present optical arrangements should be undertaken.

The observed modulation of the local transfer velocity along the wave forms shows agreement with predictions of Witting (1971). However, Witting (and subsequent investigators) assumed that sublayer thickness is controlled by processes at a phase position equivalent to the position of the mean water level. The present study supports other studies that show that high surface stresses due to wind, breaking and other processes tend to cluster near the crests of waves. Consequently, the sublayer thickness is more plausibly controlled at the wave crests and the influence of wave orbital straining is to systematically and significantly enhance transfer along the entire wave forms. A normalization based on Witting's formulation is developed to determine the wave-related enhancement of constituent exchange.

Some investigators have observed detached surface layers of constituent-rich water and have concluded that these are indicative of strong constituent flux. Such events were also observed during these present experiments but they do not exercise a strong influence on the interfacial gradient and therefore do not play a strong role in determining overall constituent flux.

With the wave-related enhancement deducted from the total exchange rate, a partition between the wave-related and turbulent/capillary ripple contributions to exchange is determined in the absence of microscale breaking. The turbulent/capillary ripple contribution is of identical form to normalizations determined by Ledwell (1984), Coantic (1986) and Jähne *et al.* (1987) with a slightly reduced coefficient of 1/17.3. It is found that the development of strong parasitic capillary waves towards the incipient breaking limit does not noticeably enhance constituent transfer.

The predictions by Peirson & Banner (2003) of a strong enhancement of low-solubility gas flux at the onset of microscale breaking are confirmed with direct observations of the concomitant onset of very thin aqueous diffusion sublayers. By deducting the wave- and turbulent/ripple-flux contributions from the total exchange rate in the presence of microscale breaking waves, it is determined that an efficiency factor of 17 % needs to be applied to Peirson & Banner's model, which is extended to field conditions. However, these present estimates of efficiency are premised on assumptions associated with visual observations of microscale breaking frequency. Quantitative methods of determining breaking efficiency have recently been developed and these present findings should be critically reviewed using such techniques.

The overall constituent exchange budget shows good collapse of the entire data set except for the special case where freely propagating wave motions are absent. The turbulent/ripple component remains the dominant contribution to the total exchange but falls to approximately 50 % of the total in the presence of well-developed microscale breaking waves. Microscale breaking plays two roles: it strongly enhances the total momentum flux to the water surface while subduction due to the breaking process itself can also enhance exchange rates by approximately 20 %. It would be valuable to determine whether similar behaviour is observed for thermal boundary layers in the presence of microscale breaking.

Substantial further work is required to apply these results to field conditions: specifically, to determine the spectral distribution of wave breaking on the surfaces of open waters and the efficiency factors applicable to larger-scale breaking waves. The strong scatter previously observed in comparisons of different sets of constituent exchange measurements are interpreted in the context of the results of this study. Surface contamination, unquantified wave orbital and breaking contributions as well as fetch dependence are all identified as potential contributors to the scatter between different experimental conditions.

Although not a central part of this investigation, bulk thermal effects were observed. While the thermal diffusion layers are presumed to have been thicker than their mass

diffusion counterparts, significant thermal influences were observed neither in the results nor in measurements made with conventional thermal probes.

Acknowledgements

Funding by the Australian Research Council under Discovery Project 0452505 for this project and ongoing support under Discovery Projects 1095722 and 0985602 is gratefully acknowledged. The late Mr John Hart made an enormous contribution to this study by manufacturing and installing much of the specialist precise equipment required. The authors would like to thank Messrs John Baird and Hector Martinez for their skilled electronic support, Margaret Titterton and Caroline Hedges for library assistance and Mrs Monika Steiler and Mrs Anna Blacka for the preparation of schematic and technical drawings. Dr Frank Bradley very kindly provided this study with a Horiba infrared sensor. W.L.P. would like to thank the Institut de Recherche sur Les Phénomènes Hors Équilibre, Marseille and particularly Dr Hubert Branger, for their hospitality during the finalization of this work. The constructive comments by the editor and three anonymous reviewers significantly improved the manuscript.

REFERENCES

APHA 1980 *Standard Methods for the Examination of Water and Wastewater*, 15th Edn. (ed. A. E. Greenberg, J. J. Connors, D. Jenkins) APHA-AWWA-WPCF.

ASCE 1984 *Standard Measurement of Oxygen Transfer in Clean Water* (ed. W. C. Boyle). ASCE.

ASHER, W., EDSON, J., MCGILLIS, W. R., WANNINKHOF, R., HO, D. T. & LITCHENDORF, T. 2002 Fractional area whitecap coverage and air-sea gas transfer velocities measured during gasex-98. In *Gas Transfer at Water Surfaces* (ed. M. A. Donelan, W. M. Drennan, E. S. Saltzman & R. Wanninkhof), Geophys. Monogr. 127, pp. 199–203. AGU.

BANERJEE, S., LAKEHAL, D. & FULGOSI, M. 2004 Surface divergence models for scalar exchange between turbulent streams. *Int. J. Multiphase Flow* **30** (7-8), 963–977.

BANNER, M. L. 1990 The influence of wave breaking on the surface pressure distribution in wind-wave interactions. *J. Fluid Mech.* **211**, 463–495.

BANNER, M. L. & PEIRSON, W. L. 1998 Tangential stress beneath wind-driven air-water interfaces. *J. Fluid Mech.* **364**, 115–145.

BANNER, M. L. & PHILLIPS, O. M. 1974 On small scale breaking waves. *J. Fluid Mech.* **65**, 647–657.

BROCCHINI, M. & PEREGRINE, D. H. 2001 The dynamics of strong turbulence at free surfaces. Part 1. Description. *J. Fluid Mech.* **449**, 225–254.

CHEUNG, T. K. & STREET, R. L. 1988 The turbulent layer in the water at an air-water interface. *J. Fluid Mech.* **194**, 133–151.

CLYMO, R. S. & GREGORY, S. P. 1975 Two cheap, temperature stable battery operated devices producing a current linearly proportional to capacitance or resistance. *J. Appl. Ecol.* **12**, 577–586.

COANTIC, M. 1986 A model of gas transfer across air-water interfaces with capillary waves. *J. Geophys. Res.* **91**, 3,925–3,943.

CRAPPER, G. D. 1957 An exact solution for progressive capillary waves of arbitrary amplitude. *J. Fluid Mech.* **2**, 532–540.

CRC 2005 *Handbook of Chemistry and Physics*, 85th edn (ed. D. R. Lide). CRC.

CSANADY, G.T. 1990 The role of breaking wavelets in air-sea gas transfer. *J. Geophys. Res.* **95**, 749–759.

DANCKWERTS, P. V. 1951 Significance of liquid-film coefficients in gas absorption. *Ind. Engng Chem.* **43**, 1460–1467.

DANIIL, E. I. & GULLIVER, J. S. 1988 Temperature dependence of liquid film coefficient for gas transfer. *J. Environ. Engng* **114**, 1224–1229.

DEACON, E. L. 1977 Gas transfer to and across an air-water interface. *Tellus* **29**, 363–374.

DEACON, E. L. 1981 Sea-air gas transfer: the wind speed dependence. *Boundary-Layer Meteorol.* **21**, 31–37.

DIORIO, J. D., LIU, X. & DUNCAN, J. H. 2009 An experimental investigation of incipient spilling breakers. *J. Fluid Mech.* **633**, 271–283.

DONELAN, M. A. 1978 Whitecaps and momentum transfer. In *Turbulent Fluxes through the Sea Surface, Wave Dynamics and Prediction* (ed. A. Favre & K. Hasselmann), Plenum.

DONELAN, M. A. 1990 Air-sea interaction. *Ocean Engng Sci.* **9**, 239–292.

DONELAN, M. A. & WANNINKHOF, R. 2002 Gas transfer at water surfaces – concepts and issues. In *Gas Transfer at Water Surfaces* (ed. M. A. Donelan, W. M. Drennan, E. S. Saltzman & R. Wanninkhof), Geophys. Monogr. 127, pp. 1–10.

DOWNING, A. L. & TRUESDALE, G. A. 1955 Some factors affecting the rate of solution of oxygen in water. *J. Appl. Chem.* **5**, 570–581.

DUNCAN, J. H., QIAO, H., PHILOMIN, V. & WENZ, A. 1999 Gentle spilling breakers: crest profile evolution. *J. Fluid Mech.* **379**, 191–222.

GEMMRICH, J. 2010 Strong turbulence in the wave crest region. *J. Phys. Oceanogr.* **40**, 583–595.

GEMMRICH, J. R., BANNER, M. L. & GARRETT, C. 2008 Spectrally resolved energy dissipation rate and momentum flux of breaking waves. *J. Phys. Oceanogr.* **38**, 1296–1312.

HIGBIE, R. 1935 The rate of absorption of a pure gas into a still liquid during short periods of exposure. *Trans. Am. Inst. Chem. Engrs* **31**, 365–389.

HOOVER, T. E. & BERKSHIRE, D. C. 1969 Effects of hydration on carbon dioxide exchange across an air-water interface. *J. Geophys. Res.* **74**, 456–464.

HUNG, L.-P. & TSAI, W.-T. 2009 The formation of parasitic capillary ripples on gravity–capillary waves and the underlying vortical structures. *J. Phys. Oceanogr.* **39**, 263–289.

JÄHNE, B. & HAUßECKER, H. 1998 Air-water gas exchange. *Annu. Rev. Fluid Mech.* **30**, 444–468.

JÄHNE, B., MUNNICH, K. O., BOSINGER, R., DUTZI, A., HUBER, W. & LIBNER, P. 1987 On the parameters influencing air-water gas exchange. *J. Geophys. Res.* **92**, 1937–1949.

JESSUP, A. T. 1996 The infrared signature of breaking waves. In *The Air-Sea Interface: Radio and Acoustic Sensing, Turbulence and Wave Dynamics* (ed. M. A. Donelan, W. H. Hui & W. J. Plant), Rosenstiel School of Marine and Atmospheric Science, University of Miami.

JESSUP, A. T. & PHADNIS, K. R. 2005 Measurement of the geometric and kinematic properties of microscale breaking waves from infrared imagery using a PIV algorithm. *Meas. Sci. Technol.* **16**, 1961–1969.

JESSUP, A. T. & ZAPPA, C. J. 1997 Defining and quantifying microscale wave breaking with infrared imagery. *J. Geophys. Res.* **102** (C10), 23145–23153.

JIRKA, G. H. & HO, A. H. W. 1990 Measurements of gas concentration fluctuations at a water surface. *J. Hydraul. Engng.* **116**, 835–847.

KAWAMURA, H., OKUDA, K., KAWAI, S. & TOBA, Y. 1981 Structure of turbulent boundary layer over wind waves in a wind tunnel. *Tohoku Geophys. J.* **28**, 69–86.

KLEISS, J. M. & MELVILLE, W. K. 2010 Observations of wave-breaking kinematics in fetch-limited seas. *J. Phys. Oceanogr.* **40**, 2575–2604.

KOMORI, S., NAGAOA, R. & MURAKAMI, Y. 1993 Turbulence structure and mass transfer across a sheared air-water interface in wind-driven turbulence. *J. Fluid Mech.* **249**, 161–183.

LEDWELL, J. J. 1984 The variation of the gas transfer coefficient with molecular diffusivity. In *Gas Transfer at Water Surfaces* (ed. W. Brutsaert & G. H. Jirka), pp. 293–302. Springer.

LEWIS, W. K. & WHITMAN, W. G. 1924 Principles of gas absorption. *Ind. Engng Chem.* **16**, 1215–1220.

LISS, P. S. 1973 Processes of gas exchange across an air-water interface. *Deep-Sea Res.* **20**, 221–238.

LISS, P. S. & MERLIVAT, L. 1986 Air-sea gas exchange rates: introduction and synthesis. In *The Role of Air-Sea Exchange in Geo-chemical Cycling* (ed. P. Buat-Menard), pp. 113–129. Springer.

LONGUET-HIGGINS, M. S. 1953 Mass transport in water waves. *Phil. Trans. R. Soc. Lond.* A **245**, 535–581.

LONGUET-HIGGINS, M. S. 1992 Capillary rollers and bores. *J. Fluid Mech.* **240**, 659–679.

LONGUET-HIGGINS, M. S. 1995 Parasitic capillary waves: a direct calculation. *J. Fluid Mech.* **301**, 79–107.

MACINTYRE, F. 1971 Enhancement of gas transfer by interfacial ripples. *Phys. Fluids* **14**, 181–184.
MCKENNA, S. P. & MCGILLIS, W. R. 2004 The role of free-surface turbulence and surfactants in air-water gas transfer. *Int J. Heat Mass Transfer* **47** (3), 539–553.
MCCREADY, M. J., VASSILIADOU, E. & HANRATTY, T. J. 1986 Computer simulation of turbulent mass transfer at a mobile interface. *AIChE Journal* **32** (7), 1108–1115.
MELVILLE, W. K. & MATUSOV, P. 2002 Distribution of breaking waves at the ocean surface. *Nature* **417**, 58–63.
MITSUYASU, H. 2009 *Looking Closely at Ocean Waves: From Their Birth to Death*. Terrapub.
MÜNSTERER, T. & JÄHNE, B. 1998 LIF measurements of concentration profiles in the aqueous mass boundary layer. *Exp. Fluids* **25**, 190–196.
PEIRSON, W. L. 1997 Measurement of surface velocities and shears at a wavy air-water interface using particle image velocimetry. *Exp. Fluids* **23**, 427–437.
PEIRSON, W. L. & BANNER, M. L. 2003 Aqueous surface layer flows induced by microscale breaking wind waves. *J. Fluid Mech.* **479**, 1–38.
PEIRSON, W. L. & GARCIA, A. W. 2008 On the wind-induced growth of slow water waves of finite steepness. *J. Fluid Mech.* **608**, 243–274.
PEIRSON, W. L., WALKER, J. W., WELCH, C. H. & BANNER, M. L. 2007 Defining the enhancement of air-water interfacial oxygen exchange rate due to wind-forced microscale waves. In *Transport at the Air Sea Interface – Measurements, Models and Parameterizations* (ed. C. S. Garbe, R. A. Handler & B. Jähne), Springer.
PHILLIPS, O. M. 1985 Spectral and statistical properties of the equilibrium range in wind-generated gravity-waves. *J. Fluid Mech.* **156**, 505–531.
QIAO, H. & DUNCAN, J. H. 2001 Gentle spilling breakers: crest flow-field evolution. *J. Fluid Mech.* **439**, 57–85.
SAYLOR, J. R. & HANDLER, R. A. 1999 Capillary wave gas exchange in the presence of surfactants. *Exp. Fluids* **27**, 332–338.
SCRIVEN, L. E. & PIGFORD, R. L. 1958 On phase equilibrium at the gas-liquid interface during absorption. *AIChE J.* **4**, 439–444.
SIDDIQUI, M. K. H. & LOEWEN, M. R. 2007 Characteristics of the wind drift layer and microscale breaking waves. *J. Fluid Mech.* **573**, 417–456.
SKJELBREIA, L. & HENDRICKSON, J. 1961 Fifth order gravity wave theory. In *Proc. 7th Int. Conf. Coastal Engng* pp. 184–196. ASCE.
SZERI, A. J. 1997 Capillary waves and air-sea gas transfer. *J. Fluid Mech.* **332**, 341–358.
TAKEHARA, K. & ETOH, G. T. 2002 A direct visualization method for CO_2 gas transfer at water surface driven by wind waves. In *Gas Transfer at Water Surfaces* (ed. M. A. Donelan, W. M. Drennan, E. S. Saltzman & R. Wanninkhof), Geophys. Monogr. 127, pp. 89–95.
THORPE, S. A. 2005 *The Turbulent Ocean*. Cambridge University Press.
TOBA, Y. & KAWAMURA, H. 1996 Wind-wave coupled downward-bursting boundary layer beneath the sea surface. *J. Phys. Oceanogr.* **52**, 409–419.
TSAI, W.-T. & HUNG, L.-P. 2011 Characteristics of gas-flux density distribution at the water surfaces. In *Gas Transfer at Water Surfaces* (ed. S. Komori & W. McGillis), Kyoto University Press, (in press).
TURNEY, D. E., SMITH, W. C. & BANERJEE, S. 2005 A measure of near-surface fluid motions that predicts air-water gas transfer in a wide range of conditions. *Geophys. Res. Let.* **32**, L04607.
VERON, F., MELVILLE, W.K. & LENAIN, L. 2008 Wave-coherent air-sea heat flux. *J. Phys. Oceanogr.* **38**, 788–802.
VERON, F., SAXENA, G. & MISRA, S. K. 2007 Measurements of the viscous tangential stress in the airflow above wind waves. *Geophys. Res. Lett.* **34**, L19603.
WALKER, J. W. 2009 The exchange of oxygen at the surface of open waters under wind forcing. PhD thesis. School of Civil and Environmental Engineering, The University of New South Wales.
WALKER, J. W. & PEIRSON, W. L. 2008 Measurement of gas transfer across wind-forced wavy air-water interfaces using laser-induced fluorescence. *Exp. Fluids* **44**, 249–259.
WANNINKHOF, R. 1992 Relationship between gas exchange and wind speed over the ocean. *J. Geophys. Res.* **97**, 7373–7381.

WANNINKHOF, R., ASHER, W. E., HO, DAVID T., SWEENEY, COLM & WADE R., MCGILLIS 2009 Advances in quantifying air-sea gas exchange and environmental forcing. *Annu. Rev. Mar. Sci.* **1**, 213–244.

WANNINKHOF, R. H. & BLIVEN, L. F. 1991 Relationship between gas exchange, wind speed, and radar backscattar in a large wind wave tank. *J. Geophys. Res.* **96**, 2785–2796.

WANNINKHOF, R. & MCGILLIS, W. R. 1999 A cubic relationship between gas transfer and wind speed. *Geophys. Res. Lett.* **26**, 1889–1892.

WITTING, J. 1971 Effects of plane progressive irrotational waves on thermal boundary layers. *J. Fluid Mech.* **50**, 321–334.

WOLFF, L. M. & HANRATTY, T. J. 1994 Instantaneous concentration profiles of oxygen absorption in a stratified flow. *Exp. Fluids* **16**, 385–392.

WOODROW, P. T. & DUKE, S. R. 2001 Laser-induced fluorescence studies of oxygen transfer across unsheared flat and wavy air-water interfaces. *Ind. Engng Chem. Res.* **40**, 1985–1995.

YAN, X., PEIRSON, W. L., WALKER, J. W. & BANNER, M. L. 2011 On transitions in the Schmidt number dependency of low solubility gas transfer across air-water interfaces. In *Gas Transfer at Water Surfaces* (ed. S. Komori & W. McGillis), pp. 355–365. Kyoto University Press.

ZAPPA, C. J., ASHER, W. E. & JESSUP, A. T. 2001 Microscale wave breaking and air-water gas transfer. *J. Geophys. Res.* **106** (C05), 9385–9391.

ZAPPA, C. J., ASHER, W. E., JESSUP, A. T., KLINKE, J. & LONG, S. R. 2004 Microbreaking and the enhancement of air-water transfer velocity. *J. Geophys. Res.* **109**, C08S16.